The Pennsylvania State University
The Graduate School
College of Engineering

PIECEWISE-LINEAR MECHANO-HYDRAULIC MODELS OF INTRACRANIAL PRESSURE DYNAMICS

A Thesis in
Engineering Science and Mechanics
by
Davis J. Evans

Submitted in Partial Fulfillment
of the Requirements
for the Degree of

Master of Science

December 2016

The thesis of Davis J. Evans was reviewed and approved* by the following:

Corina S. Drapaca
Associate Professor of Engineering Science and Mechanics
Thesis Co-Advisor

Joseph P. Cusumano
Professor of Engineering Science and Mechanics
Thesis Co-Advisor

Gary L. Gray
Associate Professor of Engineering Science and Mechanics
Thesis Committee Member

Judith A. Todd
P. B. Breneman Chair and Professor of Engineering Science and Mechanics
Department Head

*Signatures are on file in the Graduate School.

Abstract

Elevated intracranial pressure (ICP) is an extremely dangerous condition for patients who are suffering from traumatic brain injury, hydrocephalus, or related neurological disorders. To make informed decisions when treating patients, clinicians must understand how the body regulates ICP. Mathematical models can aid in this task. In addition to making quantitative predictions, accurate mathematical models can also describe the transition between different qualitative behaviors of ICP. This is crucial, because, for instance, in a pathological case known as Lundberg A-Waves, ICP oscillates between high and low pressures over a long period. This is in contrast to a healthy state, where ICP remains mostly constant with respect to time.

In this thesis, we develop mathematical models of ICP dynamics with the goal of explaining how a healthy state of constant ICP can transition to the oscillatory case of Lundberg A-Waves. These low-dimensional models are built by coupling a lumped mechanical system with a hydraulic system, and applying the first-principles of the balance of mass and the balance of linear momentum to obtain the governing equations.

The first of these models is a single-compartment model of the coupled mechanics and hydraulics of the ventricular cerebrospinal fluid (CSF) and the surrounding brain tissue. The governing equations are two coupled linear ordinary differential equations. Once we develop a nondimensional form of the governing equations, we postulate several different piecewise laws for the CSF formation rate that depend on either pressure or volume. Then, we examine the resulting piecewise-linear dynamical systems for the existence of a limit cycle. To do so, we look for fixed points in an analytic expression of the Poincaré map, which we construct as a composition of other maps represented as parametric curves. Once we determine which of these postulated CSF formation laws result in model equations that can exhibit limit cycles, we draw possible clinical conclusions based on this information.

The second model is a dual-compartment model that couples the mechanics and hydraulics of the ventricular CSF, arterial blood, and brain tissue. The governing

equations are four coupled linear ordinary differential equations. We numerically examine the stability characteristics of this linear system, once we specify values for the model parameters. In addition, we show that the steady-state ICP that the model predicts for these values agrees well with what is observed clinically.

Table of Contents

List of Figures

List of Tables

Chapter 1
Introduction

Elevated intracranial pressure (ICP) is an extremely dangerous condition for patients who are suffering from traumatic brain injury, hydrocephalus, or related neurological disorders. When the brain is incapable of lowering ICP to healthy levels, the high pressure can cause irreversible brain damage to the patient. With an understanding of the possible causes of high ICP, along with the mechanisms by which the brain regulates its pressure, doctors can make an informed decision as to the course of treatment for a patient. Mathematical models can aid in this task. Such models provide quantitative explanatory power, by offering the capability to predict ICP dynamics through simulations. In addition, these models can also describe qualitative changes in the steady-state of ICP. This is important because some pathological steady-states are non-constant. One example is the case of Lundberg A-Waves, a condition where ICP oscillates with dangerous amplitudes over a long period of about thirty minutes. This is in contrast to the otherwise-healthy condition, where ICP remains nearly constant (within a small range that follows the heartbeat). Describing both of these behaviors is one goal of the modeling work that follows.

As of yet, the most common method to model ICP dynamics has been to derive governing equations from an electric circuit analogy. In this modeling approach, electric nodes represent compartments of fluid, for example, the ventricular CSF compartment. Here, voltage is analogous to pressure, and electric current is analogous to hydraulic flow. While this treatment enforces the principle of the balance of mass, it does not respect the balance of linear momentum as applied to the

boundary of the compartment: in this case, the mass of the brain tissue. A different modeling approach used to describe ICP dynamics is through the use of continuum mechanics. These models are built by imposing the balance of mass and balance of linear momentum at a local level, and allow for a full spatial and temporal description of the pressure field. However, the apparent high precision of this method is offset due to uncertainties in geometry, proper constitutive models, and boundary conditions. In addition, because only the spatially-averaged value of ICP is of clinical use, the complexity and computational cost characteristic of these models is an unnecessary burden. In fact, a lumped-parameter model can provide us with the same information in a much simpler way.

With this in mind, we build a single-compartment linear model of the ventricular cerebrospinal fluid (CSF) that consists of a hydraulic system describing the flow of CSF, coupled to a mechanical system that describes the deformation of the surrounding brain tissue. This construction imposes both the balance of mass and the balance of linear momentum while also remaining low-dimensional. As a result, the model is governed by a set of ordinary differential equations. Once these equations are derived, we analyze their behavior, paying special attention to equilibria, stability, and bifurcations. The focus of this analysis is a search for the existence of a limit cycle, which would correspond to the oscillatory Lundberg A-Waves mentioned earlier. We immediately find that the unmodified linear model is not capable of exhibiting this behavior. From there, we postulate different piecewise laws that describe the CSF formation rate, and analyze the resulting piecewise-linear systems for the existence of limit cycles. The constitutive laws that create limit cycles can be interpreted as possible hypotheses for the underlying mechanism of Lundberg A-Waves. Finally, we derive a two-compartment model that accounts for the ventricular CSF and arterial blood compartments, as well as the surrounding tissue. From the modeling assumptions, we arrive at governing equations. Once we specify values for the model parameters, we numerically determine the stability properties of the equilibrium point. We also show that the steady-state value of intracranial pressure that the model predicts for these values agrees with what would be clinically observed in a healthy patient.

The rest of this chapter is devoted to a review of the literature, where we present brain physiology that is relevant to the modeling work to follow. This is followed up with a discussion of the achievements and limitations of the most widely-cited

models of ICP dynamics. In Chapter 2, we construct the single-compartment model of the ventricular CSF chamber, as well as analyze the possible dynamic behaviors that result from assuming a particular CSF formation rate. In Chapter 3, we construct the dual-chamber model with ventricular CSF and arterial blood compartments. Finally, in Chapter 4 we discuss the conclusions that we can draw from this work, along with their potential clinical impact.

1.1 Review of Relevant Literature

In order to appropriately model ICP dynamics, it is essential to understand certain physiological processes of the brain, and how they interface with ICP. In addition, we must also understand the different qualitative types of ICP dynamics that are observed in clinical practice. This section will present the brain physiology that is relevant to the modeling work in subsequent chapters. We follow this with a discussion of the achievements and limitations of the most prominent models existing in the current literature.

The human brain is a multi-component system comprised of cerebrospinal fluid, interstitial fluid, brain cells, and blood vessels (vasculature). On average, the brain has a mass of about 1.5 kg [1]. The majority of what is considered brain tissue consists of white matter and grey matter, which are both soft and mildy compressible [2]. The volume of the skull in an average adult is about 1475 mL. Of this amount, it contains 1300 mL of brain tissue, 65 mL of CSF, and 110 mL of blood on average [3]. While the blood is contained within blood vessels, in the *intravascular* space, CSF surrounds the brain on all sides, and is also contained in large cavities known as *ventricles* within the brain. CSF is a colorless liquid made of 99% water that fills the brain's ventricles, subarachnoid space, and intracellular space. About 80-90% of CSF is created by the *choroid epithelium*, which produces CSF on the order of a few hundred milliliters per day. The presence of this fluid introduces damping to the brain motion, which cushions and protects it from injury [4].

As well as being continually formed from the bloodstream, CSF is also continually being reabsorbed into the venous blood at a rate such that, under normal conditions, the total volume of CSF remains approximately constant [3]. There exists a relatively constant pressure difference from the inside of the brain (ventricles

containing CSF) to the outside (dura matter). This pressure gradient induces flow in CSF, causing it to be reabsorbed into the bloodstream via the venous system. Therefore, the rate of reabsorption is linked to the intracranial pressure. Above a certain value of ICP, the reabsorption rate is very nearly proportional to pressure. Although Cutler [5] states that at very low values of ICP, the absorption rate is negligible, this does not necessarily imply that the absorption rate is no longer linear. The absorption of CSF into the bloodstream, and hence, removal from the intracranial compartment, is the primary natural mechanism for lowering the intracranial pressure. As a result, abnormally high intracranial pressure is commonly caused by high resistances to resorption, which is to say there is a lower resorption rate for the same pressure gradient. For the same reason, in principle, high ICP could also be caused by an abnormally high rate of CSF production, but clinicians have found that this condition is very unlikely to occur in patients with otherwise-healthy CSF resorption rates [3].

In addition to naturally regulating ICP by regulating the volume of CSF, the brain also contains autoregulatory mechanisms that control the flow of blood in the cerebral arteries. In order to ensure a constant artery-to-vein difference in oxygen concentration, the brain automatically regulates the cerebral blood flow (CBF), by a process known as cerebral autoregulation. The cerebral arteries dilate or constrict, accordingly, to regulate the flow of blood to the brain as oxygen consumption, blood viscosity, and the cerebral profusion pressure change. The cerebral profusion pressure (CPP) is the difference between mean arterial pressure (MAP) and intracranial pressure (ICP). The current state of the research does not indicate an agreement on the precise mechanism of cerebral autoregulation [6]. The two main physiological theories include the *myogenic theory*, and the *metabolic theory*. The former indicates that changes in CBF occur due to changes in pressure, while the latter suggests that CBF autoregulation is driven by changes in CO_2 levels of arterial blood.

Lundberg A-Waves, also known as plateau waves, are long-period (approx. 30 min), high-amplitude (approx. 50 - 100mmHg) oscillations in the intracranial pressure [3]. Lundberg A-Waves frequently occur when patients suffer from high blood pressure within the brain (intracranial hypertension). However, they have been observed in otherwise-healthy patients as well as patients in critical condition. Lundberg A-Waves are a potentially dangerous condition because the resulting

high ICP can slow the blood flow to the brain, since it reduces the cerebral profusion pressure defined earlier. The mechanism by which Lundberg A-Waves are formed is currently not completely understood. The leading, albeit unproven, hypothesis relies on the brain's mechanism of cerebral autoregulation in the following sense: high ICP causes a drop in the CPP, so the brain dilates the cerebral arteries in order to keep CBF constant; this increase in cerebral blood volume causes a further increase in ICP, and so on [3]. Other types of waveforms in ICP have been observed. Other than the ever-present low-amplitude waveform that follows the heartbeat, there are also Lundberg B-Waves (1-2min period, 20-50mmHg amplitude) and Lundberg C-Waves (4-5 min period, $<$ 20 mmHg amplitude) [3]. As opposed to the A-Waves, the presence of Lundberg B- or C-Waves is likely not indicative of any pathological condition.

Changes in ICP are usually attributed to changes in volume of the main fluids contained within the skull: cerebrospinal fluid and arterial blood [3, 7, 8]. Quantifying this relationship between pressure and volume is central to most modeling efforts. The Monro-Kellie Doctrine [3], named for Alexander Monro II (1733 –1817) and his student, George Kellie (1720 - 1779), is a modeling hypothesis that idealizes the skull as rigid. More precisely, the Monro-Kellie doctrine asserts that the total volume contained within the skull cannot be changed. This simple hypothesis still remains central to modern modeling efforts, as it restricts the scope of a model to the skull alone. Because the skull cavity is made of several constitutive parts, namely CSF, blood, and brain tissue, the Monro-Kellie Doctrine has the implication that adding CSF to the cranial cavity would either cause the brain tissue to compress or cause blood to leave the skull. Such an increase in the volume of CSF is then accompanied by an increase in ICP. The relationship between CSF volume and ICP is nonlinear [7], and the research community is still making new efforts to effectively quantify this relationship. The quasi-static pressure-volume relationship is often expressed through a term known as the compliance, C, which is defined as

$$C = \frac{dV}{dP}\,, \tag{1.1}$$

where V is the volume of CSF in the cranial cavity, and P is the intracranial pressure. This term, compliance, that is used in the ICP modeling literature is not to be confused with the term of the same name in the mechanics literature, which means the inverse of stiffness. While conceptually similar, these two quantities

have different units, and therefore cannot be compared to one another directly. As a result, we only use the term compliance when examining the existing literature, and refrain from its use in our own work in order to avoid ambiguity. Initial modeling efforts by Guinane took $C = C_0$ constant [9]. Later, A. Marmarou matched experiments much more closely [7] than Guinane by proposing the following functional dependence of C:

$$C = \frac{1}{kP}\,, \tag{1.2}$$

where k is a constant with appropriate units. Lim *et al.* [10] have shown that the following form

$$C = ae^{-bP}\,, \tag{1.3}$$

where a, b are constants, also reproduces data well, if only for the fact that the functional form does not deviate much from the simpler form proposed by Marmarou.

While the compliance is a good measure of the quasi-static pressure-volume relationship, it cannot alone describe how ICP varies naturally with time. In order to describe dynamic behavior of ICP, the pressure-volume relationship must be coupled with laws describing the net change of CSF volume over time. Marmarou *et al.* [7] pioneered these studies, which were followed by Ursino *et al.* [8], and Kashif *et al.* [11], among others. Models of this type are typically referred to as compartmental models, because their construction involves balancing mass between one or more chambers (i.e., compartments) that have variable volume and pressure. The original modeling work pioneered by Marmarou required specifying a functional form for the rate of CSF production (constant) and absorption (linear with pressure) into and out of the ventricles, and balancing these flow rates with the storage according to the intracranial compliance. This construction then allows for temporal predictions of ICP as a response to a change in the volume of CSF. Later, Ursino *et al.* [8] expanded upon the work of Marmarou by introducing a two-compartment model: the ventricular CSF chamber as well as the cerebral blood chamber. In addition, this particular model [8] models the cerebral blood flow as a process that is controlled by feedback, and as a result, has the capability of exhibiting limit cycles in the state space that are intended to represent the oscillatory Lundberg A-Waves. Work by Linninger *et al.* [12] expands again upon this multi-compartmental idea. Linninger's model includes compartments

for the carteroid arteries, left and right arteries, arterioles, capillaries, veniules, and veins, jugular veins, venous sinus, and the left and right lateral ventricles, third, and fourth ventricles. Lakin et al. [13] provides yet another compartmental model of ICP dynamics, in the context of how it may be affected by the rest of the body. Lakin's model challenges the Monro-Kellie doctrine by including a compartment for extracranial CSF. However, this particular model requires 16 separate compartments in order to include the intracranial blood vessels, intracranial CSF, extracranial CSF, the heart, the blood vessels of the body, and the tissue of the rest of the body. Thus, if the Monro-Kellie doctrine is excluded from the underlying modeling assumptions, the number of equations and independent parameters rapidly expands, resulting in an unwieldy model that is not easily studied or used.

We should also note that ICP models are frequently built by constructing analogous electric circuits, where voltage represents fluid pressure and electric current represents the volume rate of flow. It follows that an electric resistor then represents pressure-driven flow through a "pipe", and a capacitor then represents storage of fluid as a direct function of pressure. However, this analogy can only be taken so far. In order to accommodate CSF, brain tissue must deform, and an electric circuit analogy does not properly describe the dynamics of deformation, which may be different than the quasi-static behavior. Both the balance of linear momentum and the balance of mass are well-established principles of physics that must be respected while modeling physical processes. A compartmental electric circuit analogy will include only the mass balance principle, because it is directly analogous to Kirchoff's current laws. However, the linear momentum balance principle will *not* be built-in if the model equations are derived directly from an electric circuit analogy. Of course, it would be possible to construct an electric circuit with an identical governing equation to the coupled mechanical and hydraulic system, however, doing so would break the original analogy: only some elements in the circuit would conform to the analogy where electric current through an element corresponds to fluid flow. In our work, we derive the governing equations directly from the balance of mass and the balance of linear momentum of a mechano-hydraulic system.

Building compartmental models is not the only method used to model ICP dynamics, as some authors have applied continuum mechanics to this problem. Hakim *et al.* [14] pioneered this approach by proposing the first continuum model

of ICP dynamics. Afterward, Nagashima *et al.* [15] carried out simulations of a continuum model by using the finite element method to solve the governing partial differential equations with a computer. Later, Sobey *et al.* [16] also developed a continuum model that could be compared to CSF infusion test experiments, where a known volume of CSF is injected and the response is measured. Models of this class are comprised by a set of partial differential equations with an associated set of boundary conditions, and therefore can describe the pressure field in space as well as time. Because these equations often do not have analytic solutions, they must be solved numerically. However, this additional spatial information comes at a high computational cost. In addition, Sobey *et al.* [16] observed that in their spherically-symmetric continuum ICP model, the pressure of CSF was nearly constant throughout the ventricles and parenchyma [16]. Their group then, by realizing that a lumped-parameter model would be quicker to solve numerically, averaged the pressure field over the space of the ventricles. In doing so, they recovered the same governing equations as the single compartment model of Marmarou. While this was not an experimental measurement – they did not measure the entire pressure field throughout the brain – this modeling exercise suggests that ICP dynamics might best be described as a set of ordinary differential equations in time, without regard to the spatial resolution of the pressure field. In fact, measuring ICP is extremely difficult, so clinical data with spatial resolution of the pressure field do not even exist, to the best of our knowledge. Instead, ICP data are interpreted as the spatially-averaged value of the pressure field throughout the ventricles. In particular, we are interested in studying the time-dependent behavior of the ICP waveform in the case of Lundberg A-Waves, but also Lundberg B- and C-Waves, as well as the return to a steady-state value of ICP after CSF injection. These temporal effects seem to occur over the entire brain, and not in a specific region. In a sense, if the only useable quantity from a model is the spatially-averaged ICP, it is unnecessary to solve partial differential equations on the entire spatial domain, only to average them later. Therefore, we believe that a lumped-parameter model could accurately describe the ICP dynamics of scientific interest, as well as of relevance to clinicians, while still being quick to solve numerically as compared to a continuum model.

One advantage of a continuum model, however, is the prediction of the deformation and stress fields throughout the brain. Unfortunately, accurately and

completely describing the mechanical properties of brain tissue required by continuum models is still an open problem. One main concern is whether the tissue is best modeled as an elastic, poroelastic, or viscoelastic material [2]. This decision is also context-dependent, where the time scale of observation may help to determine the most appropriate model [2]. Uncertainties in the constitutive behavior of tissue, the geometry, and the boundary conditions arguably make the apparent precision introduced by a continuum model illusory.

The classical Kelvin-Voigt (KV) and Kelvin-Voigt-Maxwell-Biot (KVMB) constitutive models have been used to study brain dynamics. These models idealize an finite volume of viscoelastic or poroelastic material with a discrete number of spring and dashpot elements. In the simplest, single degree of freedom case, the KV model simplifies the description of a viscoelastic material by representing the elastic component as a single spring that is in parallel with a dashpot that represents the viscous damping.

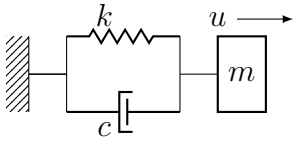

Figure 1.1: Schematic representation a Kelvin-Voigt viscoelastic solid connected to a mass m.

A pictorial representation of the KV element is shown in Fig. 1.1. The linear spring, with spring constant k, and the linear dashpot, with damping constant c, are attached in parallel to the combined mass of fluid and solid, m. The distance u represents the relative displacement to the spring's unstretched length. Considering only a single degree of freedom, the differential equation of motion is that of a damped harmonic oscillator:

$$m\frac{d^2u}{dt^2} + c\frac{du}{dt} + ku = 0\,. \tag{1.4}$$

The KV model describes viscoelastic materials well, where the difference between solid and fluid displacements are small. However, in poroelastic materials, where there are large relative displacements between the mass of solid and the mass of fluid, the KV model is insufficient to fully capture the motion of both phases. Good models of poroelasticity treat the motions of the fluid and the solid separately. In

the KVMB model, the mass of the fluid and the mass of the solid are separated and are connected to one another through a viscous damping element, and connected to ground by an elastic spring element, as illustrated in Fig. 1.2.

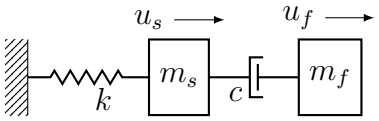

Figure 1.2: Schematic Representation of KVMB model.

In this case, the minimal model possesses two degrees of freedom, so that the balance of linear momentum yields the following system of differential equations.

$$\begin{cases} m_s \frac{d^2 u_s}{dt^2} + c\left(\frac{du_s}{dt} - \frac{du_f}{dt}\right) + k u_s = 0 \\ m_f \frac{d^2 u_f}{dt^2} + c\left(\frac{du_f}{dt} - \frac{du_s}{dt}\right) = 0\,, \end{cases} \tag{1.5}$$

where u_s, u_f are the displacements of the solid and fluid mass, respectively. While the KVMB model introduces an additional term into the model, it offers an higher level of precision when describing poroelastic materials. Under certain circumstances in the study of brain biomechanics (see [17]), the KVMB model can be well-approximated by the simpler KV model without introducing much error.

From this search of the literature, we find that the most widely-preferred way to model ICP dynamics is with lumped-parameter compartmental models. Since ICP does not vary much throughout the ventricles, it is likely unnecessary to use a continuum model, which will not only be difficult to solve, but also hard to use if one wishes to compare predicted ICP dynamics to clinical data. However, the compartmental models found in the literature are built from electric circuit analogies, and therefore do not have an equivalent analogy to the linear momentum balance law. In the next chapter, we will derive a mechano-hydraulic model that is low-dimensional, and also respects both the balance of mass and the balance of linear momentum.

Chapter 2
A Single-Reservoir Model

In this chapter, after a brief discussion, we enumerate modeling assumptions of an idealized description of the CSF stored in the ventricles. Then, by applying well-established principles of physics, we obtain governing equations for the description of the pressure and volume of ventricular CSF. We nondimensionalize the resulting equations, and explore the possible dynamic behaviors of them in the state space. Our analysis will pay particular attention to stability of equilibria and bifurcations that may have clinical meaning when explaining Lundberg A-Waves.

An effective mathematical model is an abbreviated description of reality [18]. It may seem that adding as much information as possible to a model would increase its accuracy. While potentially true, this act quickly robs the model of any explanatory power. In fact, if a mathematical model could include so much detail as to describe nature completely, it would be necessarily useless, as it would offer no benefit over studying nature itself. On the other hand, if a model is so simple that it cannot make accurate predictions, it will not be useful either. Hence, the most useful model will describe what it is built for, but as simply as possible. Such a model can then lend insight into how to interpret the physical world, which can then allow for more refined experiments to improve the model. Therefore, in order to construct a useful model, the phenomenon that is to be studied must be well-defined, so that all extraneous information may be discarded. In our case, we are interested in describing the time-series dynamics of intracranial pressure (ICP). In particular, this includes the return to a steady-state value of ICP from an external stimulus such as CSF injection, as well as the oscillatory condition of Lundberg A-Waves.

These conditions are defined by how the (spatially-averaged) ICP varies with

time, with no distinction as to how the ICP field varies with position. Therefore, a model that describes the spatial distribution of ICP includes unnecessarily detail. These reasons motivate our decision to build low-dimensional, lumped-parameter models of ICP dynamics, as opposed to infinite-dimensional continuum models. This means that the governing equations will be a set of ordinary differential equations (ODEs), as opposed to partial differential equations (PDEs). In order to completely describe the steady-state value of ICP and the oscillatory Lundberg A-Waves in a way that agrees with observations, the system of ODEs must have particular qualitative properties. To describe the healthy steady-state, solutions of the system of ODEs must approach a stable equilibrium point, while in the case of Lundberg A-Waves, solutions should approach a stable limit cycle. This behavior is only possible in nonlinear systems of ODEs. Our approach is to assume a constitutive law describing the CSF formation rate that is a nonlinear (in particular, piecewise-constant) adjustment to an otherwise-linear system. Then, we examine which constitutive laws result in qualitative dynamics that agree with observations. If a model that is built with sound physical reasoning agrees with observations, then that model may lend more physical insight than observations alone. Therefore, with the aid of the following models, we can search for an explanation as to how a stable, constant equilibrium value of ICP can transition to the oscillatory Lundberg A-Waves.

2.1 Governing Equations

This model can be thought of as coupled hydraulic and mechanical systems. The hydraulic system is an idealization of the ventricular CSF system, and is governed by the balance of mass. The mechanical system is an idealization of the brain tissue and is governed by the balance of linear momentum. These governing principles will tie together the behaviors of CSF absorption, CSF formation, and the dynamics of the surrounding brain tissue.

CSF absorption is a passive pressure-driven process that involves fluid transport between tissues. It is not simply flow through a cylindrical pipe, and it could have an arbitrary functional dependence on the pressure gradient. However, if the flow rate can be described as an algebraic function of the pressure differential, then the leading-order approximation of that function is a flow rate that is proportional

to the pressure differential. Therefore, we idealize the absorption rate of CSF as proportional to the difference between the intracranial pressure, P, and the venous blood pressure, Q. This construction was also used by Marmarou *et al.* [7] and Ursino *et al.* [8] in their electric circuit analogies, where they used an electric resistor to represent a proportional flow rate. Therefore we can interpret this proportionality constant as a volumetric fluid resistance, and write it as $1/R$, as in

$$q_{out} = \frac{P - Q}{R}\,, \tag{2.1}$$

where q_{out} is the volume rate of CSF absorption. While we write the absorption rate of CSF as proportional to this pressure gradient, we do not yet specify the form of the formation rate, q. In future sections, we will examine how different functional forms of q will affect the dynamics of the overall system. Marmarou *et al.* [7] fixed the CSF formation rate as constant, while Ursino *et al.* [8] made it proportional to the difference between the arterial blood pressure, which we are not considering in this model, and ICP. The balance of mass principle states that the net mass flow into a chamber must equal the rate of change of the stored mass. Because the fluid in question is CSF, which is mostly water, we reasonably idealize the fluid as incompressible. In addition, we state that the brain tissue surrounding the CSF-filled ventricles must always be in contact with the CSF. Therefore, any change in the volume of stored CSF must be accompanied by a deformation of the surrounding tissue. We can write this as

$$q - \frac{P - Q}{R} = \dot{V}\,, \tag{2.2}$$

where q is the volume rate of CSF formation, V is the total volume of ventricular CSF, and the overdot indicates the derivative with respect to time. Now that we have related the formation, storage, and absorption of CSF through the balance of mass (Eq. (2.2), we must specify the dynamics of the surrounding tissue. Because this model does not attempt to explain the shape brain tissue takes on while accommodating CSF, we idealize the ventricular volume as a constant surface area, A, with a generalized deformation coordinate, x. In other words, we treat the deformation of brain tissue as if it is constrained to one degree of freedom. The volume of CSF, V, is equal to $V = V_0 + Ax$, where V_0 is the undeformed ventricle volume. Because the coordinate x represents deformation, it takes the value $x = 0$

in the undeformed configuration. We further treat the surrounding tissue as a linear viscoelastic, Kelvin-Voigt solid. For our single degree of freedom system, this corresponds to the addition of a linear spring in parallel with a dashpot as shown in Fig. 2.1. The tissue that is being displaced has mass, and we lump all of this mass into a single mass element shown in Fig. 2.1. We should point out that this mass, m, is not the entire mass of the brain. Rather, it is an effective mass of the parts of the brain affected by changes in CSF volume. Thus, application of the linear momentum balance (Newton's second law of motion) on the effective mass yields

$$m\ddot{x} + \eta\dot{x} + kx = PA\,, \tag{2.3}$$

where PA is the force generated by the intracranial pressure, P, acting over the ventricle surface area, A. The two governing equations, Eqs. (2.2) and (2.3) are coupled through the terms P and $\dot{x}$. Through a simple algebraic manipulation, we can solve for P,

$$P = Rq - RA\dot{x} + Q\,, \tag{2.4}$$

and substitute it into Eq. (2.3), yielding

$$m\ddot{x} + (\eta + RA^2)\dot{x} + kx = ARq + AQ\,. \tag{2.5}$$

This linear second-order ordinary differential equation in x is known as a damped harmonic oscillator, and its solution is well-understood [19]. When a solution to Eq. (2.5) is established, we can substitute $\dot{x}$ into Eq. (2.4) to get the pressure, P.

The primary focus of the remaining analysis is to study the existence (or non-existence) of limit cycles for a prescribed q. Because the coefficient of $\dot{x}$ in Eq. (2.5) will always be positive (for positive R and A), setting $\eta = 0$ does not change the qualitative structure of the linear equation. For this reason, we take $\eta = 0$ for the remainder of the work, for we claim that it only clarifies the following analysis concerned with finding limit cycles, and will not affect the conclusions we draw.

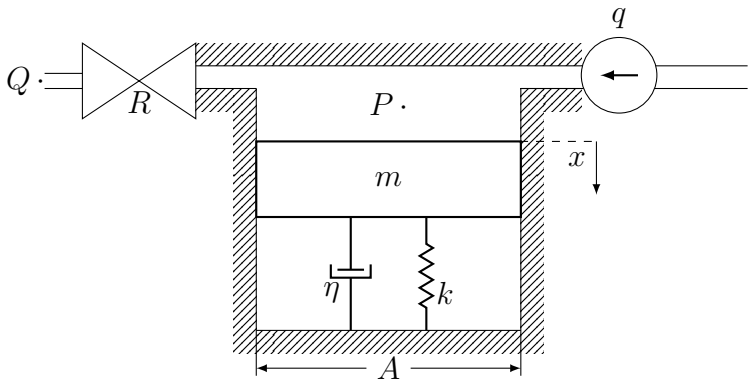

Figure 2.1: Fluid-Mechanical model of the ventricular CSF system, where m is the effective mass of the ventricle wall, k and η are the effective stiffness and damping constants of the deforming tissue, and x is its deformation. The intracranial pressure is P, Q is the venous blood pressure, q is the volumetric rate of CSF formation, A is the ventricle wall surface area. The effective spring is unstretched when $x = 0$.

2.2 Nondimensionalization of the Governing Equations

If we wish to speak of the relative size of model parameters in a way that does not depend on the choice of units, nondimensionalization of the model equations is a necessary procedure. In addition, nondimensionalization can reduce the number of independent parameters, which can clarify analysis and expedite understanding. To rescale by both length and time, let

$$x = x_c \bar{x}\,, \tag{2.6}$$

and

$$t = t_c \bar{t}\,, \tag{2.7}$$

where x_c is some characteristic length, t_c is some characteristic time, $\bar{x}$ is the dimensionless length, and $\bar{t}$ is the dimensionless time. Observe that, via the chain rule of differentiation,

$$\dot{x} = \frac{dx}{dt} = \frac{dx}{d\bar{t}}\frac{d\bar{t}}{dt} = \frac{dx}{d\bar{t}}\frac{1}{t_c}\,. \tag{2.8}$$

By substituting Eqs. (2.6) and (2.7) into the ODE (2.5), we obtain the following.

$$\frac{mx_c}{t_c^2}\frac{d^2\bar{x}}{d\bar{t}^2} + RA^2\frac{x_c}{t_c}\frac{d\bar{x}}{d\bar{t}} + kx_c\bar{x} = ARq + AQ \tag{2.9}$$

$$\frac{d^2\bar{x}}{d\bar{t}^2} + \frac{RA^2}{m}t_c\frac{d\bar{x}}{d\bar{t}} + \frac{kt_c^2}{m}\bar{x} = \frac{t_c^2}{mx_c}\left(ARq + AQ\right) \tag{2.10}$$

Because we are free to choose the characteristic time t_c, we let

$$t_c = \sqrt{\frac{m}{k}}\,. \tag{2.11}$$

Similarly, we choose x_c to be

$$x_c = \frac{QA}{k}\,. \tag{2.12}$$

These scalings naturally give rise to related scalings of the flow q and resistance R. Let the dimensionless flow $\bar{q}$ be defined as

$$\bar{q} = \frac{R_c q}{Q} \tag{2.13}$$

and the dimensionless fluid resistance $\bar{R}$ be defined

$$\bar{R} = \frac{R}{R_c} \tag{2.14}$$

where R_c is defined as

$$R_c = \frac{\sqrt{mk}}{A^2}\,. \tag{2.15}$$

With these definitions, elementary algebraic manipulations from Eq. (2.5) will result in the following re-scaled, dimensionless equation.

$$\frac{d^2\bar{x}}{d\bar{t}^2} + \bar{R}\frac{d\bar{x}}{d\bar{t}} + \bar{x} = \bar{R}\bar{q} + 1 \tag{2.16}$$

With this choice of units, the value of the outlet pressure Q is always scaled to 1, because $\frac{x_c m}{t_c^2 A} = Q$. Therefore, we can interpret Q as the characteristic pressure in this particular scaling, and thus take

$$P = \bar{P}Q\,, \tag{2.17}$$

where $\bar{P}$ is the dimensionless intracranial pressure. From Eq. (2.4), we obtain the following expression for the dimensionless pressure.

$$\bar{P} = \bar{R}\bar{q} + 1 - \bar{R}\frac{d\bar{x}}{d\bar{t}} \tag{2.18}$$

The use of these rescaled equations is predicated upon the parameters A, k, m, and Q remaining constant with respect to time. However, we can study behaviors of this system with non-constant $\bar{R}$ and $\bar{q}$, as we will in the following sections. All of our remaining work will be with the dimensionless equations. **At this point, it is common practice to "drop the bars"**; in other words, we redefine x to mean the dimensionless length, redefine t to mean the dimensionless time, etc. Our system is now the following two equations, where $\dot{x} = \frac{dx}{dt}$ is the derivative of the dimensionless length with respect to the dimensionless time.

$$\boxed{\ddot{x} + R\dot{x} + x = Rq + 1} \tag{2.19}$$

$$\boxed{P = Rq + 1 - R\dot{x}} \tag{2.20}$$

This particular scaling is helpful if we want to examine the effects of flow rate and resistance changing with state, as we intend to do. If we would want the spring-rate or outlet pressure, for example, to change with state, a different scaling might possibly be more helpful. To determine the intracranial pressure, P, the second-order ODE of Eq. (2.19) can be solved for $x(t)$ and $\dot{x}(t)$, independently of P. Then, the corresponding pressure waveform $P(t)$ is obtained by substituting $\dot{x}(t)$ into Eq. (2.20). Because $P(t)$ and $x(t)$ are related through this transformation, qualitative features – such as number and location of equilibria, as well as the existence of limit cycles – that are understood in the $(x, \dot{x})$ plane are likely to retain their character in the (x, P) plane. However, this may not necessarily be the case if q is allowed to vary with state, as we will see in the following sections.

2.3 Behavior of the Linear System

The simplest form that we can impose on R and q is that they remain constant with respect to time, position, and pressure. Once we take R and q as constants, Eq. (2.19) becomes a second-order linear ordinary differential equation with con-

stant coefficients. The behavior of these equations are well-understood. The possible behaviors can be determined by writing the ODE in state-variable form, $\dot{\mathbf{u}} = \mathsf{A}\mathbf{u}$, and then examining the eigenvalues of the matrix A. Let $u = x-(Rq+1)$, and $\dot{u} = v$. Substitution into Eq. (2.19) yields

$$\begin{aligned} \dot{u} &= v \\ \dot{v} &= -u - Rv \end{aligned} \tag{2.21}$$

which can be written in matrix form as

$$\dot{\mathbf{u}} = \mathsf{A}\mathbf{u}\,, \tag{2.22}$$

where $\mathbf{u} = \begin{pmatrix} u \\ v \end{pmatrix}$, and $\mathsf{A} = \begin{pmatrix} 0 & 1 \\ -1 & -R \end{pmatrix}$.
An individual time-series solution $(u(t), v(t))$ to the ODE (2.22) can be plotted as a parametric curve in the phase-space, which in this case is the (u, v) plane. The solution, when plotted in this way, is referred to as either a phase-path or trajectory. The phase-space is an extremely useful tool because solutions to initial-value problems (an ODE with given initial conditions) are *unique*. Geometrically, this has the important implication that in the phase-space, trajectories may never cross. This allows us to use geometrical arguments to shed light on the possible solutions that a system may express.

Equilibrium points of the system occur where $\dot{u} = 0$ and $\dot{v} = 0$. For this system, there is only one equilibrium point, which is at the origin: $u = 0$, $v = 0$. The type of solution can be either exponential or sinusoidal, since the general solution to this system is

$$u(t) = C_1 e^{\lambda_1 t} + C_2 e^{\lambda_2 t}\,, \tag{2.23}$$

where C_1 and C_2 are constants prescribed by initial conditions, and $\lambda_{1,2}$ are the eigenvalues of the matrix A, found by solving its characteristic equation,

$$\det\left(\mathsf{A} - \lambda \mathsf{I}\right) = 0\,. \tag{2.24}$$

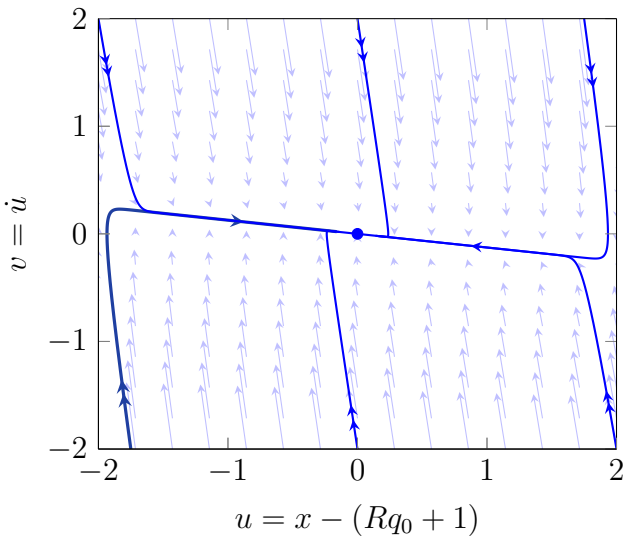

Figure 2.2: Phase portrait of the linear system, when $\varphi = 4$, and $q_0 = 1$. Every solution path approaches the origin as $t \to \infty$.

In this case, the eigenvalues are

$$\lambda_{1,2} = -\varphi \pm \sqrt{\varphi^2 - 1}\,, \tag{2.25}$$

where $\varphi = \frac{1}{2}R$. Figure 2.2 shows a representative phase portrait for this linear system, when $\varphi > 1$. Because P is merely a linear transformation of $\dot{x}$, it also approaches a constant value as $t \to \infty$. A representative time-series solution for P is shown in Figure 2.3. Physically, this would indicate that given any perturbation in either velocity or position, the system will self-equilibriate. However, this system cannot exhibit limit cycles, as it is linear. The only type of solutions permissible are either the stable node (shown), or a stable focus when $\varphi < 1$, if we only consider positive parameter values. The following sections impose piecewise laws that govern the CSF formation rate, q, as possible mechanisms to explain the experimentally-observed periodic solutions.

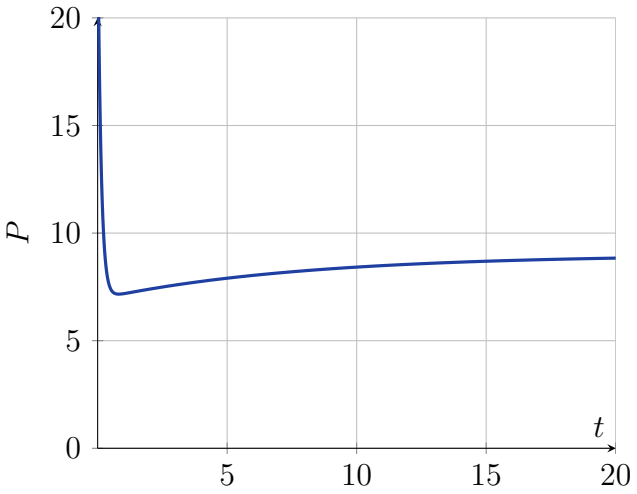

Figure 2.3: Time-series plot of Pressure for the linear system. Because $P = 2\varphi q_0 - 2\varphi\dot{x} + 1$, the pressure approaches an equilibrium value just like $\dot{x}$ does.

2.4 Pressure-Dependent CSF Formation Rate

In this section, we postulate the following behavior of CSF formation. Let

$$q = \begin{cases} q_0 & : P < \psi \\ 0 & : P \geq \psi \end{cases}, \tag{2.26}$$

where $\psi > 1$ is some critical threshold pressure that exceeds the outlet pressure (recall that the outlet pressure Q has been re-scaled to 1). This law that governs q may be interpreted as a hypothesis of the mechanism by which CSF is formed in the brain, where the CSF formation rate "shuts off" once ICP exceeds some critical threshold.

After substituting Eq. (2.26) into the governing equation, Eq. (2.19), will assume the form of two different, distinct linear systems, depending on the value of P. Because P is an algebraic function of $\dot{x}$, we can establish the boundaries to these regions in the $(x, \dot{x})$ plane, so we can study the dynamics that result from these piecewise laws. Let $\Omega_A = \{(x, \dot{x}) \in \mathbb{R}^2 \mid P < \psi\}$. By Eq. (2.20), we are in Ω_A when

$$Rq + 1 - R\dot{x} = P < \psi \tag{2.27}$$

and since $q = q_0$ in Ω_A,

$$\dot{x} > q_0 + \frac{1 - \psi}{R}, \tag{2.28}$$

and it is equivalent to write $\Omega_A = \{(x, \dot{x}) \in \mathbb{R}^2 \mid \dot{x} > q_0 + \frac{1-\psi}{R}\}$. Let $\Omega_B = \{(x, y) \in \mathbb{R}^2 \mid P \geq \psi\}$. Similarly by Eq. (2.20),

$$Rq + 1 - R\dot{x} = P \geq \psi \tag{2.29}$$

and since $q = 0$ in Ω_B,

$$\dot{x} \leq \frac{1 - \psi}{R}, \tag{2.30}$$

so it is equivalent to write $\Omega_B = \{(x, y) \in \mathbb{R}^2 \mid \dot{x} \leq \frac{1-\psi}{R}\}$. After resolving the inequalities (2.28) and (2.30), we find that law (2.26) results in two separate regions of the phase space that are not connected! In other words, there are points in the phase space $(x, \dot{x})$ that belong to neither Ω_A nor Ω_B. This is illustrated in Figure

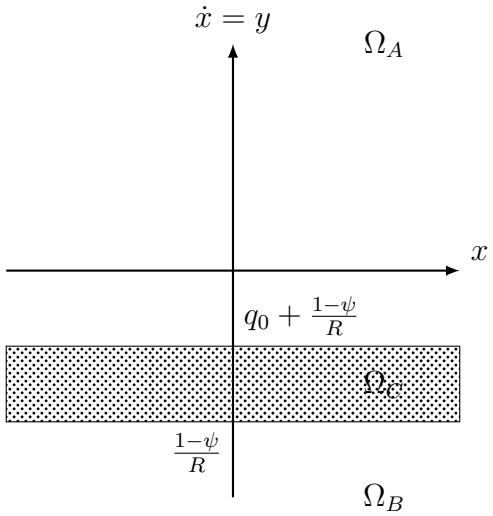

Figure 2.4: Illustration of the three regions for the piecewise-linear system. Equation (2.26) is insufficient to define the system over the entire $(x, \dot{x})$ plane: it describes it for only Ω_A and Ω_B. Instead, we prescribe the law in Eq. (2.31) so that region Ω_C is defined as well.

2.4. In order for motions to be physically-meaningful, they must have continuous positions x and also continuous velocities $\dot{x}$ with respect to time. Currently, we have no law that describes how the state evolves if $\frac{1-\psi}{R} \leq \dot{x} \leq \frac{1-\psi}{R} + q_0$. In order to continue, we must re-pose (2.26) in a way that enforces the continuity of q. Instead, let q be prescribed by

$$q = \begin{cases} q_0 & : P < \psi - \epsilon \\ \frac{-q_0}{2\epsilon}(P - \psi) + \frac{q_0}{2} & : \psi - \epsilon \leq P \leq \psi + \epsilon \\ 0 & : P > \psi + \epsilon \end{cases}, \tag{2.31}$$

where $\varepsilon > 0$. With this law, we can resolve the boundaries in the $(x, \dot{x})$ plane as follows. Redefine $\Omega_A = \{(x, \dot{x}) \in \mathbb{R}^2 \mid P < \psi\}$, and by Eq. (2.20), in a way similar to before, we have

$$\dot{x} > q_0 + \frac{1 - \psi + \epsilon}{R}, \tag{2.32}$$

when $P < \psi - \epsilon$, and we can equivalently write $\Omega_A = \{(x, \dot{x}) \in \mathbb{R}^2 \mid \dot{x} > q_0 + \frac{1-\psi+\epsilon}{R}\}$. Similarly, redefine $\Omega_B = \{(x, \dot{x}) \in \mathbb{R}^2 \mid P > \psi\}$, and by Eq. (2.20),

$$\dot{x} < \frac{1 - \psi - \epsilon}{R}, \tag{2.33}$$

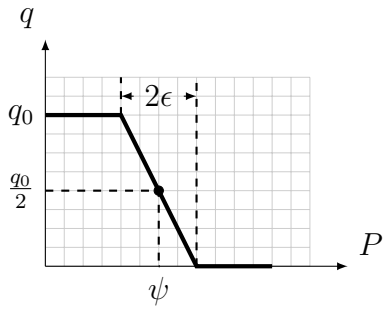

Figure 2.5: Illustration of CSF formation rate q prescribed by Eq. (2.31).

when $P > \psi + \epsilon$, and we can equivalently write $\Omega_B = \{(x, \dot{x}) \in \mathbb{R}^2 \mid \dot{x} < \frac{1-\psi-\epsilon}{R}\}$. Then, we define $\Omega_C = \{(x, \dot{x}) \in \mathbb{R}^2 \mid \psi - \epsilon \leq P \leq \psi + \epsilon\}$. To equivalently write this as a boundary in the $(x, \dot{x})$ plane, we must first eliminate P from the expression of the flow q in Eq. (2.31):

$$q = \frac{q}{2\epsilon}\left(\frac{\epsilon + \psi - 1 + R\dot{x}}{1 + \frac{Rq_0}{2\epsilon}}\right), \tag{2.34}$$

which can then be used to resolve the inequalities from in the region Ω_C after some algebra:

$$\frac{1-\psi-\epsilon}{R} \leq \dot{x} \leq q_0 + \frac{1-\psi+\epsilon}{R}, \tag{2.35}$$

and then we can equivalently write $\Omega_C = \{(x, \dot{x}) \in \mathbb{R}^2 \mid \frac{1-\psi-\epsilon}{R} \leq \dot{x} \leq q_0 + \frac{1-\psi+\epsilon}{R}\}$. With q established by (2.31), we now see that the phase-space is separated into three distinct regions: these regions cover the entire $(x, \dot{x})$ plane, and also do not overlap. In other words, each point $(x, \dot{x}) \in \mathbb{R}^2$ belongs to one and only one region, either Ω_A, Ω_B, or Ω_C. By substituting the value of q according to the region, we obtain the following three ODEs, one for each region of the phase space.

$$\ddot{x} + R\dot{x} + x = Rq_0 + 1 \qquad \text{in } \Omega_A \tag{2.36}$$

$$\ddot{x} + R\dot{x} + x = 1 \qquad \text{in } \Omega_B \tag{2.37}$$

$$\ddot{x} + \frac{R}{1+\alpha}\dot{x} + x = \frac{\alpha}{1+\alpha}(\psi - 1 + \epsilon) + 1 \quad \text{in } \Omega_C, \tag{2.38}$$

where $\alpha = \frac{Rq_0}{2\epsilon}$. If we were to consider each linear ODE on its own, over the entire $(x, \dot{x})$ plane, they would all be globally-stable linear systems, because we only allow $R > 0$ and $\alpha > 0$. This can be quickly verified by computing the eigenvalues as

before. Every solution would asymptotically approach the equilibrium point as $t \to \infty$. However, in a piecewise-linear dynamical system, each linear domain does not necessarily need to contain its own equilibrium point. In particular, every linear system from Eqs. (2.36), (2.37), and (2.38) contains exactly one equilibrium point, each of which is on the x-axis. However, because of how we have defined the boundaries to Ω_A, Ω_B and Ω_C, only one of these three regions will contain the x-axis. Therefore we say that only one region will contain its own equilibrium point. If we are to observe behavior other than asymptotic stability in this piecewise-linear system, it will be due to the interaction of the three systems with each other. The remainder of this analysis is carried out with the intent to find conditions under which a steady-state periodic solutions can exist.

Since equations (2.36), (2.37), and (2.38) are all linear, they each contain exactly one equilibrium point, which does not necessarily lie within its own region, as specified earlier. For example, in Ω_A, the equilibrium point occurs at the point $(x_{eq}, y_{eq}) = (Rq_0 + 1, 0)$. By its definition, all points in Ω_A must satisfy $\dot{x} > q_0 + \frac{1-\psi+\epsilon}{R}$, so if $q_0 + \frac{1-\psi+\epsilon}{R} > 0$, the x-axis is not included, and therefore this point is in Ω_C, and not Ω_A. Furthermore, the equilibrium point of each linear system is located on the x-axis (where $\dot{x} = 0$). Therefore, because the region boundaries are lines of constant y, we conclude that the piecewise-linear system may contain only one of the three equilibria, because only one region, either Ω_A, Ω_B, or Ω_C, may contain the x-axis. Each linear system also possesses its own qualitative behavior, which can be determined via the eigenvalues of its system matrix. For regions Ω_A and Ω_B:

$$\lambda_{1,2} = -\varphi \pm \sqrt{\varphi^2 - 1}\,. \tag{2.39}$$

The limit cycles, if they exist, should occur even when the ODEs on Ω_A (normal behavior) describe an overdamped harmonic oscillator. Lundberg A-Waves are observed on very long time scales – on the order of 30 minutes – and therefore are unlikely to be an artifact of underdamped oscillations. This motivates the following restriction on φ. We let

$$\boxed{\varphi > 1} \tag{2.40}$$

from this point forward. We justify this assumption in the same way we justify

not considering negative parameters. The expectation that our system is stable under normal operation limits φ to positive values, and the expectation that it is overdamped under normal operation requires $\varphi > 1$. To further clarify our search for limit cycles, we propose the following two lemmas.

Lemma 2.4.1 *The region Ω_B cannot contain an equilibrium point.*

Proof Because the governing ODEs for region Ω_B are linear, there is only one equilibrium point of those ODEs. Furthermore, in order for $\dot{x} = 0$, the equilibrium point must be on the x-axis. However, Ω_B does not contain any points along the x-axis, as this would require

$$\begin{aligned} \dot{x} = 0 &< \frac{1 - \psi - \epsilon}{R} \\ \psi - 1 &< -\epsilon \,, \end{aligned} \tag{2.41}$$

which, of course, is not possible if we require $\psi > 1$ and $\epsilon > 0$. □

Lemma 2.4.2 *A limit cycle in the piecewise-linear system* (2.36) (2.37), (2.38) *cannot exist between two regions if one of the regions contains its own equilibrium point, where that equilibrium point is a stable node.*

Proof A limit cycle, if it were to exist, cannot exist entirely in a linear region, as we have seen that these solutions are not permissible. Therefore, this type of solution, if it were to exist, must traverse through two or more regions. Let us only consider the case when Ω_A contains its own equilibrium point. First, assume the contrary –that a limit cycle traverses both regions Ω_A and Ω_C. By resolving the y-component of the flow along the boundary, we find that this component is

$$\dot{y}\big|_{y=q_0+\frac{1-\psi+\epsilon}{R}} = -x + \psi - \epsilon \tag{2.42}$$

and that the flow enters region Ω_A at an x-value that is less than the x-value for which it exits. Therefore, in order for flow to enter and then exit, it must be in the region where $\dot{x} > 0$, i.e., above the x-axis. If this were to be the case, the trajectory would encircle the node equilibrium of Ω_A by an angle of at least π radians, which would require it to cross through the span of a stable eigenvector. Since the solution must be unique, the trajectories cannot cross in the phase-plane,

which leads to a contradiction. We conclude that if Ω_A contains its own equilibrium point, a limit cycle cannot exist. We can prove something similar for when Ω_C contains its own node equilibrium point. $\square$

In order to continue looking for limit cycles, Lemma 2.4.2 tells us to not consider cases where Ω_A contains the x-axis, as we have stated earlier that it is always a stable node. Since we have shown in Lemma 2.4.1 that Ω_B cannot contain the equilibrium, we will now only consider the case when Ω_C contains the equilibrium. Furthermore, we also require that Ω_C is not a node, by Lemma 2.4.2. Even with $\varphi > 1$, Ω_C may either be a stable focus or a stable node, depending on the value of α. Because the eigenvalues of (2.38) are

$$\lambda_{1,2} = \frac{-\varphi}{1+\alpha} \pm \sqrt{\left(\frac{\varphi}{1+\alpha}\right) - 1}\,, \tag{2.43}$$

this requires

$$\frac{\varphi^2}{(1+\alpha)^2} < 1 \quad \Longleftrightarrow \quad 1 - \frac{q_0}{\epsilon} < \frac{1}{\varphi}\,. \tag{2.44}$$

In the limit $\epsilon \ll 1$,condition (2.44) is necessarily satisfied, since $\varphi > 1$. The governing equation in region Ω_C, Eq. (2.38), becomes

$$\ddot{x} + \frac{2\epsilon}{q_0}\dot{x} + x = \psi\,. \tag{2.45}$$

A limit cycle cannot exist entirely in one region, since each region is linear. Therefore, if a limit cycle were to exist, it must overlap two or more regions. There are only two possible mechanisms by which a limit cycle could exist here. One possibility, illustrated by Figure 2.6 is the case of the limit cycle existing between regions Ω_A and Ω_C. This case is equivalent to the case of a limit cycle existing between regions Ω_B and Ω_C, which we will show later. Figure 2.7 illustrates the possibility of the limit cycle encircling all three regions. Such a limit cycle would start in, say, region Ω_A, then would enter Ω_C, then Ω_B, then Ω_C, and back to Ω_A. Before we begin the analysis on these cases, we demonstrate the analytic methods that we are about to use.

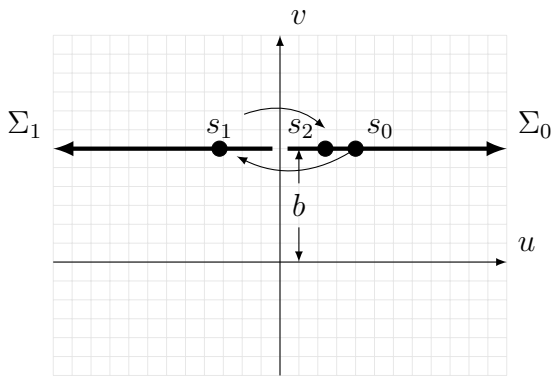

Figure 2.6: The Poincaré section $\Sigma_0 = \{(u, v) \mid u > 0, v = b\}$, where $s_0 = u$ is complimented by the second section $\Sigma_1 = \{(u, v) \mid u < 0, v = b\}$, where $s_1 = -u$. The Poincaré map $\Pi_C : \Sigma_0 \to \Sigma_1$ relates s_0 with s_1., and $\Pi_A : \Sigma_1 \to \Sigma_0$ relates s_1 with s_2. The composition of these two maps, $\Pi = \Pi_A \circ \Pi_C$, is the Poincaré map. Pragmatically, we work with the maps $\Pi_C : \Sigma_0 \to \Sigma_1$ and $\Pi_A : \Sigma_1 \to \Sigma_0$.

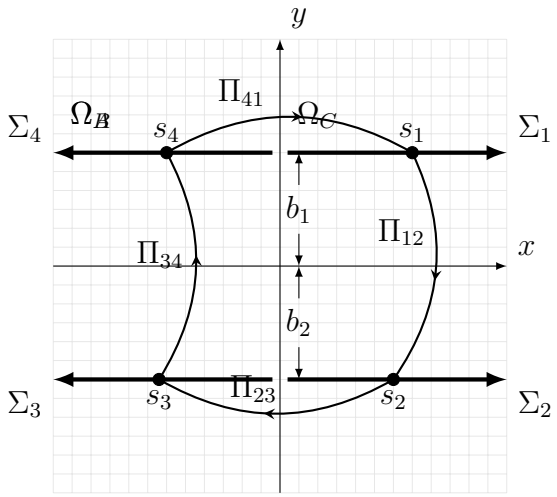

Figure 2.7: The Poincaré map $\Pi : \Sigma_1 \to \Sigma_1$ is the composition of the maps $\Pi_{41} \circ \Pi_{34} \circ \Pi_{23} \circ \Pi_{12}$.

2.4.1 Using Poincaré Maps to Find Limit Cycles

Now, we introduce the methods for limit cycle detection through use of two examples. The first example is adopted from Jordan & Smith [19]. Consider the following system of ordinary differential equations:

$$\dot{x} = \mu x + y - x\sqrt{x^2 + y^2}\,, \tag{2.46}$$

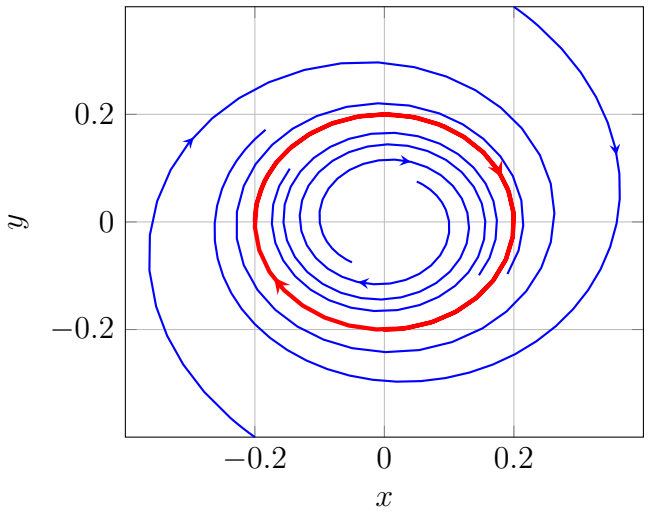

Figure 2.8: This is a phase portrait of the system (2.46), (2.47) , where $\mu = 0.2$. Note that a limit cycle passes through the point $(x, y) = (0.2, 0)$.

$$\dot{y} = -x + \mu y - y\sqrt{x^2 + y^2}\,. \tag{2.47}$$

We want a method to determine whether this system has a limit cycle. First, we select a Poincaré section Σ, a curve in the phase space that is transverse to the flow at every point [19]. We will select $\Sigma = \{(x, y) \mid x > 0, y = 0\}$. We can quickly check by plugging in $y = 0$ into Eq. (2.47) that the flow is transverse to Σ (in this case $\dot{y} \neq 0$) for the case of both $x > 0$ and $y = 0$ —we have ensured that the flow always intersects Σ in the same direction. Note that this selection of Σ is not unique, there are many other sections with these properties, which will also work.

Now that we have selected an appropriate Poincaré section, we study the behavior of solutions that leave Σ and return to Σ at a later time. In particular, we seek the map $\Pi : \Sigma \to \Sigma$, known as the Poincaré map. This map is determined uniquely by selecting a point (x_0, y_0) in Σ, and following the flow until it intersects again, at (x_1, y_1), also in Σ. Then, $(x_1, y_1) = \Pi(x_0, y_0)$. An important property of the Poincaré map is that a fixed point $(x^*, y^*) = \Pi(x^*, y^*)$ corresponds to a limit cycle in the original system, meaning our problem is now reduced to an algebra problem.

We can directly find the Poincaré map for this simple example by converting to polar coordinates (r, θ). After applying the transformation $r = \sqrt{x^2 + y^2}$, and $\theta = \arctan(y/x)$, to Eqs. (2.46) and (2.47), our system becomes

$$\dot{r} = r\,(\mu - r)\,, \quad \dot{\theta} = -1\,. \tag{2.48}$$

With initial conditions $r(0) = r_0$ and $\theta(0) = \theta_0$, we find the solutions

$$r(t) = \frac{\mu r_0}{r_0 + (\mu - r_0)e^{-\mu t}}, \quad \theta(t) = -t + \theta_0\,. \tag{2.49}$$

Because we have the exact solutions, we can write down the exact expression for the Poincaré map, since solutions that begin on Σ when $t = 0$ return to Σ again when $t = 2\pi$. The Poincaré map is the following:

$$r_1 = \frac{\mu r_0}{r_0 + (\mu - r_0)e^{-2\mu\pi}} = \Pi(r_0)\,. \tag{2.50}$$

In Fig. 2.9, we plot the Poincaré map. This plot, referred to by Andronov *et al.* as Lamerey's diagram [20], is an intuitive way to visualize repeated applications of the Poincaré map. An application of the Poincaré map can be visualized by following a given r_0 vertically until it intersects the curve $r_1 = \Pi(r_0)$. A re-application of Π can be visualized by following this intersection horizontally to the curve $r_1 = r_0$, and then vertically again as before. Since fixed points in Π correspond to cases where $r_0 = \Pi(r_0)$, we can identify these points quickly in Fig. 2.9 by looking for where the curve $r_1 = \Pi(r_0)$ intersects the line $r_0 = r_1$. We can see that one occurs where $r_0 = \mu$. This corresponds to a limit cycle passing through Σ at $r = 0.2$, which matches what we observe the phase portrait, shown in Fig. 2.8. In addition, the stability of the limit cycle can also be read from Lamerey's diagram. After each subsequent application of the Poincaré map , the value of r_1 approaches 0.2, which means that the fixed point at 0.2 is stable. In the original system, this means that solutions that do not begin on the limit cycle will eventually approach it.

We can also apply the concept of the Poincaré map to the problem of finding limit cycles in piecewise-linear systems. Since the governing set of differential equations changes depending on the region, the Poincaré map is best represented as the composition of two or more maps that describe how a trajectory enters and leaves a linear region. The previous example, however, was facile in the sense that we could write the Poincaré map in closed form. Usually, this cannot be done, as it requires solving transcendental equations, which is hard to do even for linear differential equations. However, it is usually comparatively easy to write them as

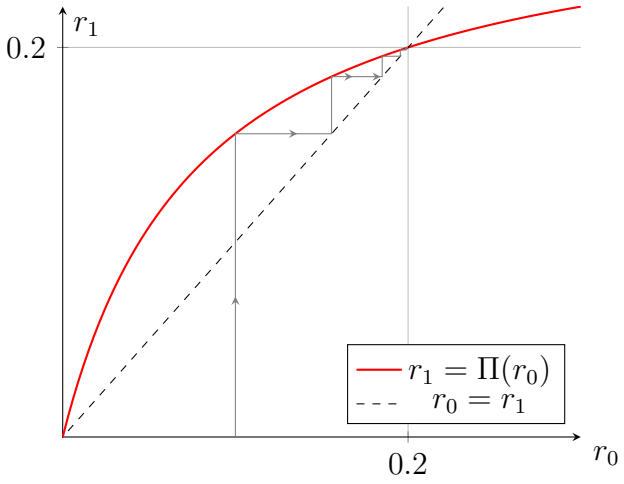

Figure 2.9: The Lamerey's diagram of the system (2.46), (2.47) , where $\mu = 0.2$. The red curve P is a plot of the Poincaré map, as written in Eq. (2.50). An application of the Poincaré map is illustrated by the vertical thin grey line. To apply the Poincaré map again, follow the grey line horizontally to the curve $r_0 = r_1$ and then vertically to the curve $r_1 = \Pi(r_0)$ once again. The fixed point of Π corresponds to the intersection of the curve $r_1 = \Pi(r_0)$ with the line $r_0 = r_1$. This fixed point occurs at $r_0 = 0.2$, and it is stable, as solutions approach it upon repeated applications of the map Π.

a parametric curve, as follows:

$$\Pi_1 : \begin{cases} s = f_1(t) \\ s' = g_1(t)\,, \end{cases} \tag{2.51}$$

$$\Pi_2 : \begin{cases} s = f_2(t) \\ s' = g_2(t)\,, \end{cases} \tag{2.52}$$

where we use the coordinates s and s' to describe the location on Σ and Σ', respectively. When written in this way, these maps are sometimes referred to as correspondence functions. Because the Poincaré map $\Pi = \Pi_2 \circ \Pi_1$, places where the parametric curves Π_1 and Π_2 cross correspond to fixed points in the Π, and therefore to limit cycles in the surrounding phase-space. To illustrate this method, now consider the following piecewise-linear system of ODEs, adopted from Andronov et al. [20]:

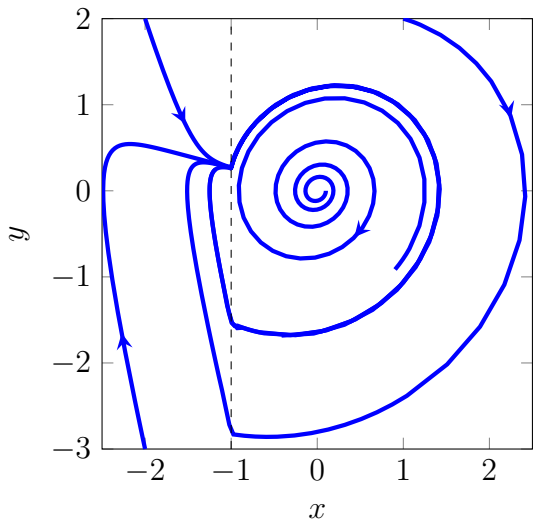

Figure 2.10: Phase portrait for the system of Eq. (2.53), where $h_1 = 2$, $h_2 = 0.1$.

$$\begin{aligned} \ddot{x} + 2h_1\dot{x} + x &= 0 \qquad x < -1 \\ \ddot{x} - 2h_2\dot{x} + x &= 0 \qquad x > -1\,, \end{aligned} \tag{2.53}$$

where $h_1 > 1$, and $h_2 < 2$. We select the Poincaré sections $\Sigma = \{(x, y) \mid x = -1, y < 0\}$ and $\Sigma' = \{(x, y) \mid x = -1, y > 0\}$, where $y = \dot{x}$. For convenience, let $s = -y$ on Σ and let $s' = y$ on Σ'. To write the maps $\Pi_1 : \Sigma \to \Sigma'$ and $\Pi_2 : \Sigma' \to \Sigma$ in closed form would be an arduous process that is not illustrative. However, we can easily represent these maps as a parametric curve. This requires solving the ODEs in (2.53) with the initial conditions $x(0) = -1, y(0) = -s$, and then setting $t = t_1$ that satisfies $x(t_1) = -1, y(t_1) = s'$. The solutions yield the map

$$\Pi_1 : \begin{cases} s = \dfrac{e^{\gamma_1\tau_1} - \cosh\tau_1 - \gamma_1 \sinh\tau_1}{\sqrt{\gamma_1^2 - 1}\sinh\tau_1} \\ s' = \dfrac{e^{-\gamma_1\tau_1} - \cosh\tau_1 + \gamma_1 \sinh\tau_1}{\sqrt{\gamma_1^2 - 1}\sinh\tau_1}\,, \end{cases} \tag{2.54}$$

where $\gamma_1 = \frac{h_1}{\sqrt{h_1^2-1}}$, and $\tau_1 = \sqrt{h_1^2 - 1}t_1$, as long as $h_1 > 1$.

Similarly, we may obtain the map

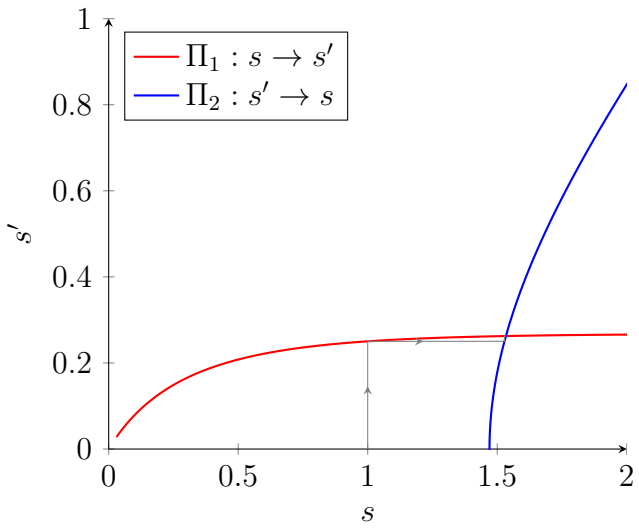

Figure 2.11: Lamerey's diagram of the system of Eq. (2.53) , where $h_1 = 2$, $h_2 = 0.1$. There is a fixed point of the Poincaré map where the two curves cross.

$$\Pi_2 : \begin{cases} s = -\dfrac{e^{\gamma_2 \tau_2} - \cos\tau_2 - \gamma_2 \sin\tau_2}{\sqrt{1+\gamma_2^2}\sin\tau_2} \\ s' = -\dfrac{e^{-\gamma_2 \tau_2} - \cos\tau_2 + \gamma_2 \sin\tau_2}{\sqrt{1+\gamma^2}\sin\tau_2} \end{cases}, \tag{2.55}$$

where $\gamma_2 = \frac{h_2}{\sqrt{1-h_2^2}}$, and $\tau_2 = \sqrt{h_2^2 - 1}t_2$. For cases where we cannot or do not wish to write the Poincaré map in closed form as in Eq. (2.50), we can graphically analyze two maps, Π_1 and Π_2 that, when composed, recover the Poincareé map Π. The two maps Π_1 and Π_2 are plotted in Fig. 2.11,

These two maps are plotted in Fig. 2.11. Because the two curves cross each other, this indicates a fixed point in the Poincaré map, which means that there exists a limit cycle in the surrounding phase space, seen in Fig. 2.10.

2.4.2 Case 1: A Limit Cycle Encircling Two Regions

Now, we apply the methods that we have previously illustrated to our original piecewise-linear system (2.36), (2.37), (2.38), in order to study the existence (or nonexistence) of a limit cycle. The first possibility for a limit cycle that we consider is the case of it existing between regions I and II, illustrated by Figure 2.6. First, define the new coordinates

$$u = x - \psi \tag{2.56}$$

$$v = \dot{u}\,, \tag{2.57}$$

which shifts the equilibrium point of region Ω_C to the origin. Let

$$b = q_0 + \frac{1-\psi}{R}\,, \tag{2.58}$$

as this allows us to rewrite the governing ODEs compactly as follows.

$$\begin{aligned} \ddot{u} + 2\varphi\dot{u} + u &= 2\varphi b \qquad \text{in } \Omega_A \\ \ddot{u} + 2\varphi\dot{u} + u &= 2\varphi(b - q_0) \qquad \text{in } \Omega_B \\ \ddot{u} + 2\gamma\dot{u} + u &= 0 \qquad \text{in } \Omega_C\,, \end{aligned} \tag{2.59}$$

where we define $\gamma = \frac{\epsilon}{q_0}$. Now, we must select a suitable subset of the (u, v) plane to act as the Poincaré section. A convenient location is the boundary between regions Ω_A and Ω_C, which is the line where $v = q_0 + \frac{1-\psi}{R} = b$. An appropriate section is one where the flow is transverse, and not tangent, to the section. We must now analyze the sign of the component of the flow that is normal to the section. In particular, this is the sign of $\dot{v}$ along $v = b$.

$$\begin{aligned} \dot{v}|_{v=b} &= -u \qquad \Omega_A \\ \dot{v}|_{v=b} &= -2\gamma b - u \qquad \Omega_C \end{aligned} \tag{2.60}$$

We see that, in Ω_A, the direction of the flow is outwards (down) when $u > 0$, and inwards (up), when $u < 0$. In Ω_C, the direction of the flow is inwards (down) when $u > -2\gamma b$, and outwards (up) when $u < -2\gamma b$. This motivates the following definitions. Let $\Sigma_0 = \{(u, v) \mid u > 0, v = b\}$, and $\Sigma_1 = \{(u, v) \mid u < -2\gamma b, v = b\}$. By considering the direction of the flow near these sections, we find that solutions

may only enter Ω_C through Σ_0, and may only enter Ω_A through Σ_1. In addition, on Σ_0, let $s_0 = u$, and on Σ_1, let $s_1 = -u$, and note that $s_0, s_1 > 0$.

We now apply the methods illustrated at the beginning of this section to directly obtain Π_A. This can be done by directly solving the linear system on Ω_A, with appropriately placed boundary conditions. The general solution to the governing equation on Ω_A, given in Eq. (2.59) is

$$u(t) = K_1 e^{(\varphi+\omega_2)t} + K_2 e^{(\varphi-\omega_2)t} + 2\varphi b\,, \tag{2.61}$$

where $\omega_2 = \sqrt{\varphi^2 - 1}$, and K_1, K_2 are arbitrary constants prescribed by initial conditions. This can also be written with hyperbolic trigonometric functions as follows

$$u(t) = e^{-\varphi t}\left(C_1 \cosh \omega_2 t + C_2 \sinh \omega_2 t\right)\,, \tag{2.62}$$

where C_1 and C_2 are different arbitrary constants prescribed by initial conditions. Because $v = \dot{u}$, Eq. (2.62) requires that

$$v(t) = e^{-\varphi t}\left((-\varphi C_1 + \omega_2 C_2)\cosh \omega_2 t + (\omega_2 C_1 - \varphi C_2)\sinh \omega_2 t\right)\,. \tag{2.63}$$

With a prescribed initial condition, we can solve for the constants C_1 and C_2. Because the system is autonomous, the value of time for the initial condition does not matter, so we pick $u(0) = u_0$, $v(0) = v_0$. Thus,

$$C_1 = u_0 - 2\varphi b\,, \tag{2.64}$$

$$C_2 = \frac{v_0 + \varphi\left(u_0 - 2\varphi b\right)}{\omega_2}\,. \tag{2.65}$$

The solution is then

$$u(t) = e^{-\varphi t}\left(\left(u_0 - 2\varphi b\right)\cosh \omega_2 t + \left(\frac{v_0 + \varphi\left(u_0 - 2\varphi b\right)}{\omega_2}\right)\sinh \omega_2 t\right)\,, \tag{2.66}$$

$$v(t) = e^{-\varphi t}\left(v_0 \cosh \omega_2 t + \left(\frac{-u_0 - \varphi v_0 + 2\varphi b}{\omega_2}\right)\sinh \omega_2 t\right)\,. \tag{2.67}$$

We now have the solution for any initial conditions. We are interested in solutions that begin on Σ_2, and then cross Σ_1 at some point in the future: let $u_0 = -s_2$, and $v_0 = b$. We also let $t = t_2$, at which, the solution crosses Σ_1, satisfying $u(t_2) = s_1$

and $v(t_2) = b$. After these substitutions into Eqs. (2.66) and (2.67), we have

$$u(t_2) = s_1 = e^{-\varphi t_2}\left((-s_2 - 2\varphi b)\cosh\omega_2 t_2 + \left(\frac{b + \varphi\,(-s_2 - 2\varphi b)}{\omega_2}\right)\sinh\omega_2 t_2\right), \tag{2.68}$$

$$v(t_2) = b = e^{-\varphi t}\left(b\cosh\omega_2 t + \left(\frac{s_2 - \varphi b + 2\varphi b}{\omega_2}\right)\sinh\omega_2 t\right). \tag{2.69}$$

Eqs. (2.68) and (2.69) form a linear system in s_1 and s_2. After careful algebraic manipulation, we can solve the linear system for s_1 and s_2, arriving at the correspondence function representation of the map Π_A.

$$\Pi_A : \begin{cases} s_1 = b\dfrac{e^{-\xi_A\tau_A} - \cosh\tau_A + \xi_A\sinh\tau_A)}{\sqrt{\xi_A^2 - 1}\sinh\tau_A} \\ s_2 = b\dfrac{e^{\xi_A\tau_A} - \cosh\tau_A - \xi_A\sinh\tau_A)}{\sqrt{\xi_A^2 - 1}\sinh\tau_A} \end{cases}, \tag{2.70}$$

where $\xi_A = \frac{\varphi}{\omega_A} = \frac{\varphi}{\sqrt{\varphi^2-1}}$, and $\tau_A = \omega_A t_A$. Because $\varphi > 1$, $\xi_A \in (1, \infty)$.

If we perform identical actions on Ω_C, we can obtain the correspondence function representation of the map Π_C:

$$\Pi_C : \begin{cases} s_1 = b\dfrac{-e^{\xi_C\tau_C} + \cos\tau_C - \xi_C\sin\tau_C)}{\sqrt{\xi_C^2 + 1}\sin\tau_C} \\ s_2 = b\dfrac{-e^{-\xi_C\tau_C} + \cos\tau_C + \xi_C\sin\tau_C)}{\sqrt{\xi_C^2 + 1}\sin\tau_C} \end{cases}, \tag{2.71}$$

where $\xi_C = \frac{\gamma}{\omega_C} = \frac{\gamma}{\sqrt{1-\gamma^2}}$, and $\tau_C = \omega_C t_C$. Although we understand that the map Π_C is one-to-one, this representation contains periodic functions, and therefore multiple values of s_2 for the same s_1. We eliminate this discrepancy by only considering the value of (s_1, s_2) corresponding to the minimum value of τ_2, for a given s, which must lie between π and 2π.

If there is a limit cycle in this piecewise-linear system, then there will be a fixed point in the Poincaré map Π. However, because $\Pi = \Pi_C \circ \Pi_A$, this problem is reduced to the problem of finding points where the curves Π_A and Π_C cross in the (s_1, s_2) plane. By numerically plotting these two curves, as we have done in Fig. 2.12, we find that this is not possible for all admissable values of φ and γ.

It is clear that the curves Π_A and Π_C approach one another as γ decreases, and when φ decreases. However, even in the limit where $\gamma \to 0$ and when $\varphi \to 1$, the

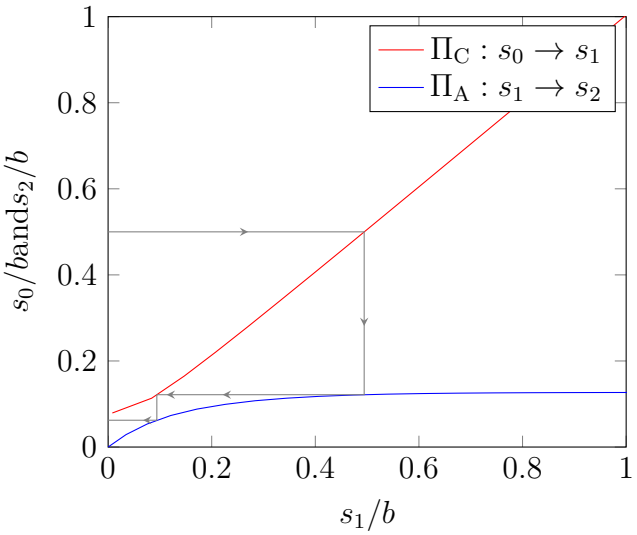

Figure 2.12: Lamerey's Diagram for the Piecewise-Hysteretic pressure-dependent system, where $\xi_C = 0.0005$, and where $\xi_A = 1.0328$. Given an initial $s_0 \in \Sigma_0$, the map Π_C will tell where this solution will cross Σ_1. Then, the map Σ_A gives the point s_2 where this solution again crosses Σ_0. This process can be repeated *ad infinitum* by first applying $s_2 \to s_0$. We find that these two curves will never cross for admissible values of ξ_A and ξ_C, and therefore this mechanism is not possible of exhibiting a limit cycle. Instead, all solutions will spiral inward to the region Ω_C, and eventually never re-enter Ω_A. In other words, after subsequent mappings, there will be a value of s_0 that will not be mapped into an s_1 via the map Π_C.

curves do not intersect anywhere except zero, which isn't a periodic orbit anyway. This corresponds to the point $(0, b)$ on both sections, which would be a boundary equilibrium point.

For completeness, we must also address the possibility of a limit cycle emerging between regions Ω_B and Ω_C. Rather than recomputing the correspondence functions for region Ω_B, we simply observe that we can recover the governing ODE of Ω_A from the ODE of region Ω_B by the substitution $(u, v) \to (-u, -v)$ and $b_2 \to b_1$, where $b_1 = b = q_0 + \frac{1-\psi}{R}$, and $b_2 = b - q_0 = \frac{1-\psi}{R}$. Since the exact value of b was immaterial from our analysis (we could scale each map by b), we recover identical correspondence functions, and therefore we reach the same conclusion: **no limit cycles may exist between regions Ω_B and Ω_C, either**.

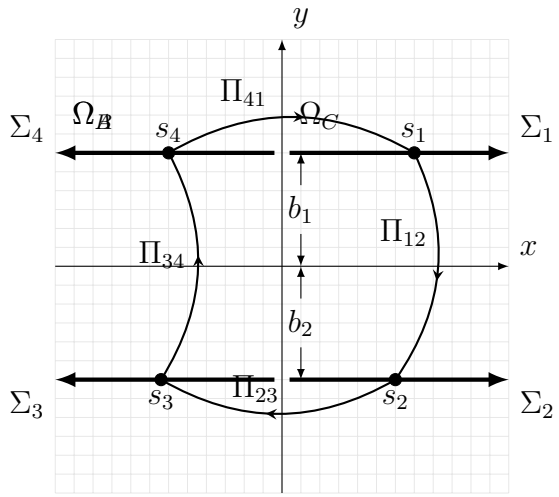

Figure 2.13: The Poincaré map $\Pi : \Sigma_1 \to \Sigma_1$ is the composition of the maps $\Pi_{41} \circ \Pi_{34} \circ \Pi_{23} \circ \Pi_{12}$. (Reproduced for clarity)

2.4.3 Case 2: A Limit Cycle Encircling Three Regions

The only remaining possibility for a limit cycle to exist in this system is the case of it passing through all three regions. Thus, the Poincaré map Π for this mechanism, illustrated in Fig. 2.13, can be written as the composition of four maps:

$$\Pi = \Pi_{41} \circ \Pi_{34} \circ \Pi_{23} \circ \Pi_{12} \,, \tag{2.72}$$

where $\Sigma_1 = \{(x, \dot{x}) \in \mathbb{R}^2 | x > 0, \dot{x} = b_1\}$, $\Sigma_2 = \{(x, \dot{x}) \in \mathbb{R}^2 | x > 0, \dot{x} = b_2\}$, $\Sigma_3 = \{(x, \dot{x}) \in \mathbb{R}^2 | x < 0, \dot{x} = b_2\}$, $\Sigma_4 = \{(x, \dot{x}) \in \mathbb{R}^2 | x < 0, \dot{x} = b_1\}$, and $b_1 = q_0 + \frac{1-\psi}{R}$, $b_1 > 0$, $b_2 = \frac{1-\psi}{R}$, $b_2 < 0$, and $\Pi_{ij} : \Sigma_i \to \Sigma_j$ is prescribed by the governing system of ODEs of Eq. 2.59. This mechanism is illustrated in Fig. 2.13. If we take the limit of $\epsilon \to 0$, we can directly obtain the two maps Π_{12} and Π_{34} in closed-form, which will expedite our analysis. Intuitively, if we find that a limit cycle does not exist for $\epsilon \to 0$, we would not expect it to exist as ϵ grows larger, as the governing system over Ω_C becomes more stable, and solutions tend inward toward the origin. In this limit, the governing equation for Ω_C becomes

$$\ddot{u} + u = 0 \quad \text{in } \Omega_C. \tag{2.73}$$

We can then show that the phase-paths in Ω_C are perfect circles. Since $\dot{u} = v$,

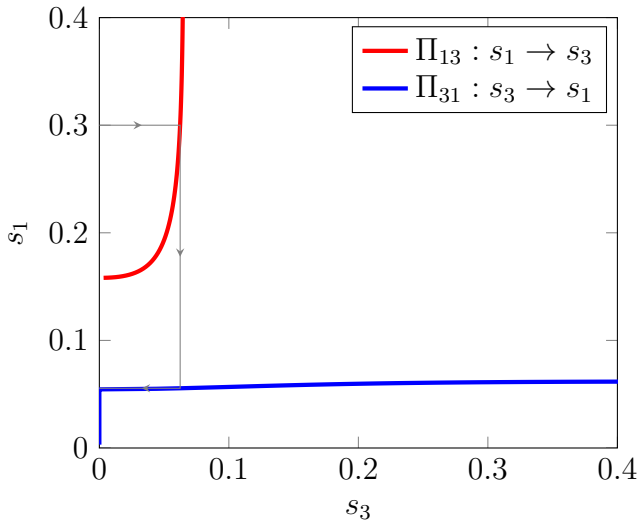

Figure 2.14: Lamerey's Diagram for possible limit cycles that pass through all three regions in the pressure-dependent system, where $\epsilon \to 0$, $\psi = 5.1$, $\varphi = 4$, and $q_0 = 1$. Because these two parametric curves do not cross, there is not a limit cycle for this configuration. In addition, we cannot find such a case for any admissable values of ψ, φ, and q_0.

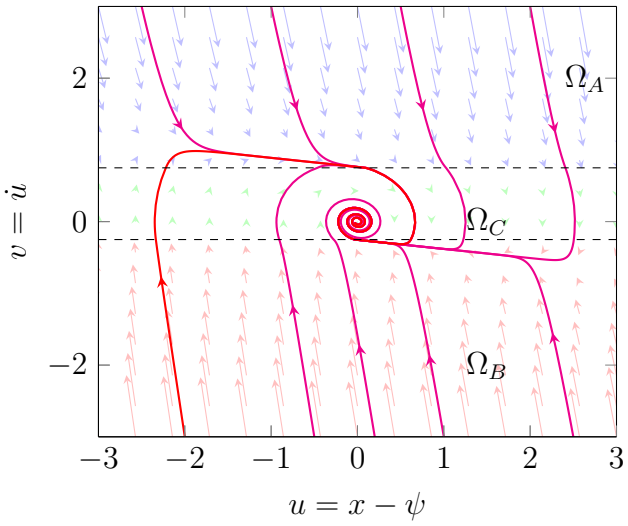

Figure 2.15: Phase portrait of the piecewise-linear system, when $\varphi = 4$, $q_0 = 1$, $\psi = 3$, and $\epsilon = 0.1$. The phase plane is separated into three regions: Ω_A, Ω_B, and Ω_C. The linear systems that govern Ω_A and Ω_B are both stable nodes, and all solutions would approach an equilibrium point on the u-axis. However, once the solution enters region Ω_C, the linear system changes to a stable focus, and the solutions tend to spiral inward toward the equilibrium point at the origin.

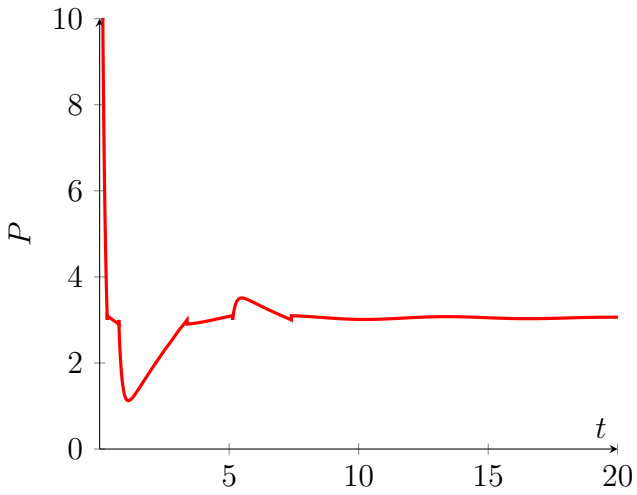

Figure 2.16: Time-series plot of pressure for the solution that begins at $(u, v) = (-2, 3)$ in Fig. 2.15. The solution rapidly decays from its initial value, and then undergoes nonlinear oscillations before settling upon the stable steady-state equilibrium value of pressure.

we have

$$\frac{\dot{v}}{\dot{u}} = \frac{dv}{du} = \frac{-u}{v}\,. \tag{2.74}$$

This differential equation can be solved as follows.

$$\int v\,\mathrm{d}v = \int -u\,\mathrm{d}u \tag{2.75}$$

$$C(u, v) = u^2 + v^2 = const. \tag{2.76}$$

Therefore, paths in Ω_C preserve the value of C over the entire solution. The circle $C(u, v)$ upon which a path enters Ω_C will be the same circle that it exits. If a path enters Ω_B at $(u, v) = (s_1, b_1) \in \Sigma_1$, it will exit at $(u, v) = (s_2, b_2) \in \Sigma_2$. If it does not, then it either approaches the equilibrium, which means it does not approach a limit cycle, or it exits through Σ_4, and therefore has been analyzed in Section 2.4.1. Therefore, we may write

$$C(s_1, b_1) = C(s_2, b_2) \tag{2.77}$$

$$s_1^2 + b_1^2 = s_2^2 + b_2^2\,, \tag{2.78}$$

which implies

$$s_2 = +\sqrt{s_1^2 + b_1^2 - b_2^2}\,. \tag{2.79}$$

The equation above is the map Π_{12} written explicitly in the form $s_2 = \Pi_{12}(s_1)$. Similarly, we can write Π_{34} as

$$s_4 = +\sqrt{s_3^2 - b_1^2 + b_2^2}\,. \tag{2.80}$$

Because Π_{12} and Π_{34} are known in closed-form, it is trivial to compose them with the maps Π_{23} and Π_{41}. If we let $\Pi_{31} = \Pi_{41} \circ \Pi_{34}$ and $\Pi_{13} = \Pi_{23} \circ \Pi_{12}$, then we can write

$$\Pi_{31} : \begin{cases} s_3 = \sqrt{\left(b_1 \dfrac{e^{-\xi\tau} - \cosh\tau + \xi\sinh\tau}{\sqrt{\xi^2-1}}\right)^2 + b_1^2 - b_2^2} \\ s_1 = \dfrac{b_1\left(e^{\xi\tau} - \cosh\tau - \xi\sinh\tau\right)}{\sqrt{\xi^2-1}\sinh\tau} \end{cases}, \tag{2.81}$$

$$\Pi_{13} : \begin{cases} s_1 = \sqrt{\left(b_2 \dfrac{e^{-\xi\tau} - \cosh\tau + \xi\sinh\tau}{\sqrt{\xi^2-1}}\right)^2 - b_1^2 + b_2^2} \\ s_3 = \dfrac{-b_2\left(e^{\xi\tau} - \cosh\tau - \xi\sinh\tau\right)}{\sqrt{\xi^2-1}\sinh\tau} \end{cases}. \tag{2.82}$$

Clearly the Poincaré map $\Pi = \Pi_{31} \circ \Pi_{13}$. Similar to the method of Section 2.4.1, we can graphically analyze the two parametric curves Π_{31} and Π_{13}, noting that crossing points correspond to limit cycles in the (u, v) plane. These curves are plotted in Fig. 2.14 with a representative set of parameters. We find that in the $\epsilon \to 0$ case, these curves do not cross for any realistic (positive) parameter values, and therefore an isolated periodic orbit is never possible in this system. If we allow ϵ to increase, we do not expect this fact to change, as solutions will have a higher tendency to approach the equilibrium point in Ω_C, with the rest of the system remaining unchanged. A representative phase portrait is shown in Fig. 2.15, and a representative pressure waveform is shown in Fig. 2.16. In the phase plane, region Ω_C clearly resembles a stable focus for this parameter configuration, while regions Ω_A and Ω_B are stable nodes that do not contain their own equilibrium point. The time-series solution for the pressure resembles a nonlinear oscillation back to a steady-state constant equilibrium.

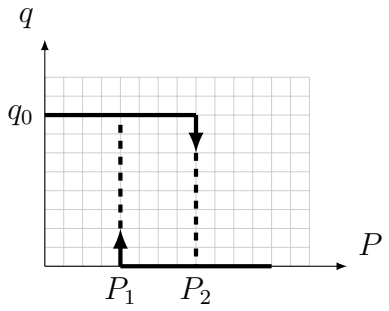

Figure 2.17: The flow is allowed to vary hysteretically with pressure. In the regions of overlap ($P_1 < P < P_2$), q retains its previous value.

2.5 Pressure-Dependent CSF Formation Rate (Hysteretic)

In this section, let q depend on pressure in the following way

$$q = \begin{cases} q_0 & : P < P_2 \\ 0 & : P > P_1, \end{cases} \tag{2.83}$$

where P_1 and P_2 are some fixed critical transition pressures satisfying $P_1 < P_2$, and q takes its previous value in the multiply-defined region, where $P_1 < P < P_2$. Therefore, if $q = q_0$,

$$P = Rq_0 - R\dot{x} + 1 < P_2 \tag{2.84}$$

$$\dot{x} > q_0 + \frac{1 - P_2}{R}\,, \tag{2.85}$$

and when $q = 0$,

$$P = -R\dot{x} + 1 > P_1 \tag{2.86}$$

$$\dot{x} < \frac{1 - P_1}{R}\,. \tag{2.87}$$

An interesting case arises when $P_2 - P_1 > Rq_0$ that we will consider now. The separation of the state-space brought forth by this results in two sheets, $\mathcal{S}_A$ and $\mathcal{S}_B$, that overlap each other in the region $q_0 - \frac{P_2 - 1}{R} < \dot{x} < \frac{-(P_1 - 1)}{R}$. This idea is

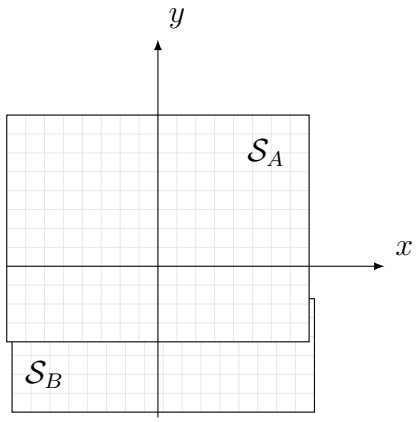

Figure 2.18: The phase space is made of two overlapping sheets. Solutions that begin on Sheet $\mathcal{S}_A$ remain on sheet $\mathcal{S}_A$, until y reaches $y = q_0 + \frac{1-P_2}{R}$, at which point they fall onto sheet $\mathcal{S}_B$.

illustrated in Figure 2.18. A solution beginning on sheet $\mathcal{S}_A$ will remain on sheet $\mathcal{S}_A$, even in the overlap region, as long as $y > q_0 - \frac{P_2-1}{R}$. As soon as $y = q_0 - \frac{P_2-1}{R}$, the governing equation immediately changes to that of sheet $\mathcal{S}_B$, with the same (x, y) coordinates as when it left sheet $\mathcal{S}_B$. The solution then remains on sheet $\mathcal{S}_B$, provided $y < -\frac{P_1-1}{R}$. As a result, although the governing equation is piecewise, the resulting solution must be continuous in both x and y.

Each sheet contains a linear system with one equilibrium point. Let us only consider the case where $P_1, P_2 > 1$. This means that the switching pressures are higher than the outlet venous pressure. If this is the case, then sheet $\mathcal{S}_B$ cannot contain its own equilibrium point, as that would require $0 < \frac{-(P_1-1)}{R}$. If this is the case, along with $P_2 - P_1 > Rq_0$, then we always have

$$0 > q_0 + \frac{1 - P_2}{R}\,, \tag{2.88}$$

which we know is always true because

$$P_2 - 1 > P_2 - P_1 > Rq_0\,, \tag{2.89}$$

which means that sheet $\mathcal{S}_A$ must always contain its own equilibrium point. If this is the case, then solutions that begin on $\mathcal{S}_A$ must either approach the equilibrium, or exit sheet $\mathcal{S}_A$, entering sheet $\mathcal{S}_B$. However, because sheet $\mathcal{S}_B$ is linear, stable, and does not contain its equilibrium, all solutions must exit in finite time, returning to

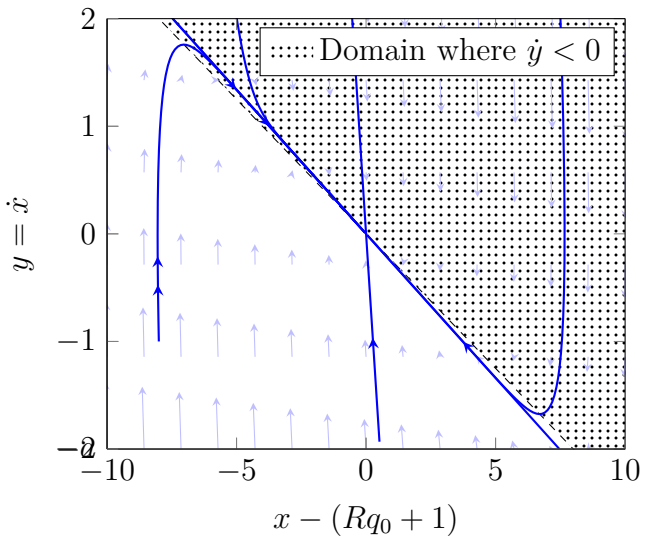

Figure 2.19: Solutions enter sheet $\mathcal{S}_A$ where $\dot{y} > 0$.In order for the solution to leave $\mathcal{S}_A$, it must have $\dot{y} < 0$. However, the solution cannot cross into the region where $\dot{y} < 0$ (the dotted region) without crossing the span of a stable eigenvector, which is not possible. Therefore, a steady-state periodic solution cannot exist, as all solutions that enter $\mathcal{S}_A$ stay there for all time.

sheet $\mathcal{S}_A$. Because we are interested in finding solutions that are periodic in the steady-state, we want to know if it is possible for the flow that enters sheet $\mathcal{S}_A$ from sheet $\mathcal{S}_B$ to exit once again. A limit cycle is possible only if this is possible. To investigate this, let us find the region of the boundary of sheet $\mathcal{S}_A$ where the flow is outward ($\dot{v} < 0$). Let $\frac{-(P_1-1)}{R} = -b < 0$, and let $q_0 - \frac{P_2-1}{R} = -a < -b < 0$. The boundary of sheet $\mathcal{S}_A$ is where $y = a$, where $\dot{y}$ is

$$\dot{y}|_{\mathcal{S}_A\ ,y=-a} = (R\,(q_0 + a) + 1) - x\,, \tag{2.90}$$

and, therefore, flow may only exit ($\dot{y} < 0$) where $x > R(q_0 + a) + 1 = P_2$. Flow may only enter sheet $\mathcal{S}_A$ where it leaves sheet $\mathcal{S}_B$, which occurs at $y = -b$. The sign of $\dot{y}$ dictates where this can occur, and we find that at $y = -b$,

$$\dot{y}|_{\mathcal{S}_B\ ,y=-b} = 1 + Rb - x\,, \tag{2.91}$$

so for flow to enter sheet $\mathcal{S}_A$ once again ($\dot{y} > 0$), we must have $x < 1 + Rb = P_1$.We can separate sheet $\mathcal{S}_A$ into two regions: one where $\dot{y} > 0$, and one where $\dot{y} < 0$.

These are separated by the locus of points where $\dot{y} = 0$, which is

$$y = \frac{-1}{R}x + \left(q_0 + \frac{1}{R}\right) . \tag{2.92}$$

Because $\dot{y}|_{\mathcal{S}_A} > \dot{y}|_{\mathcal{S}_B}$ everywhere, flow may only enter sheet $\mathcal{S}_A$ where $\dot{y} > 0$ on sheet $\mathcal{S}_A$. To exit once again, flow must somehow cross the line $y = \frac{-1}{R}x + \left(q_0 + \frac{1}{R}\right)$. Since the side $\dot{y} < 0$ lies to the left of this line, in order to cross it, we must have $\dot{x} > 0$, at this point. Since this is in the (x, y) plane, this only occurs in the top half-plane, which is above the equilibrium point. However, flow that travels this way will encircle the equilibrium point, which is not possible if $\varphi > 1$. It would need to intersect the invariant manifolds that are the spans of the eigenvectors. Therefore, we conclude that this system cannot exhibit limit cycles.

2.6 Volume-Dependent CSF Formation Rate (Hysteretic)

Once again, consider the ODE

$$\ddot{x} + R\dot{x} + x = Rq + 1 \, , \tag{2.93}$$

where this time, we let

$$q = \begin{cases} q_0 & : x < a \\ 0 & : x > b \end{cases} , \tag{2.94}$$

where $b < a$, and q takes its previous value if $b < x < a$. Like in Sec. 2.5, this choice of q separates the phase-space into two sheets: sheet $\mathcal{S}_A$ where $x < a$, and sheet $\mathcal{S}_B$ where $x > b$. In the region $x \in (b, a)$, knowledge of the previous state – and in particular, knowledge of which sheet – is necessary to predict the future dynamics. Substituting for q into the governing ODE yields two different ODEs depending on which sheet the condition is on:

$$\begin{cases} \ddot{x} + R\dot{x} + x = Rq_0 + 1 & : \quad \text{in } \mathcal{S}_A \\ \ddot{x} + R\dot{x} + x = 1 & : \quad \text{in } \mathcal{S}_B \end{cases} . \tag{2.95}$$

Each governing ODE, if considered separately, is stable. Once again, we will only

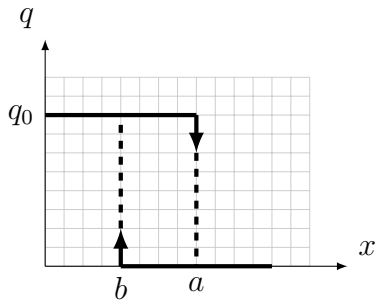

Figure 2.20: The flow is allowed to vary hysteretically with position. In the regions of overlap ($b < P < a$), q retains its previous value.

consider the case of $\varphi > 1$, so each sheet is always a stable node. Since each sheet is linear, the only two possibilities for solutions which begin on one sheet, say sheet $\mathcal{S}_A$, is to approach the equilibrium point on sheet $\mathcal{S}_A$, or leave sheet $\mathcal{S}_A$ and enter sheet $\mathcal{S}_B$.

Lemma 2.6.1 *If either sheet, $\mathcal{S}_A$ or $\mathcal{S}_B$, contains its own equilibrium point, a limit cycle cannot exist in system* (2.95)*.*

Proof Consider flow entering $\mathcal{S}_A$. This requires $y < 0$. For a limit cycle to exist, flow must exit $\mathcal{S}_A$ once again, as a limit cycle cannot exist entirely within a linear system. To exit $\mathcal{S}_A$, we would need $y > 0$, and therefore, at some point, we must cross upwards through the x-axis. This can only happen if $\dot{y} > 0$ at the point of intersection. The only points on $\mathcal{S}_A$ where both $y = 0$ and $\dot{y} > 0$ occur where $x < Rq_0 + 1$. This implies that we must cross to the left of the equilibrium point in order to exit once again, and therefore, must encircle the stable node. We know this is not possible, as it requires crossing one or more invariant manifolds. □

From Lemma 2.6.1, we take as a necessary condition that neither sheet may contain its own equilibrium point for a limit cycle to exist. This requires the following two conditions:

$$\begin{cases} a < Rq_0 + 1 \\ b > 1 \end{cases} . \tag{2.96}$$

Let us pick values of a and b that not only satisfy the condition in Eq. (2.96), but also are symmetric about some axis. This symmetry is not a necessary condition to observe the behavior that is to follow, but it allows for a cleaner and

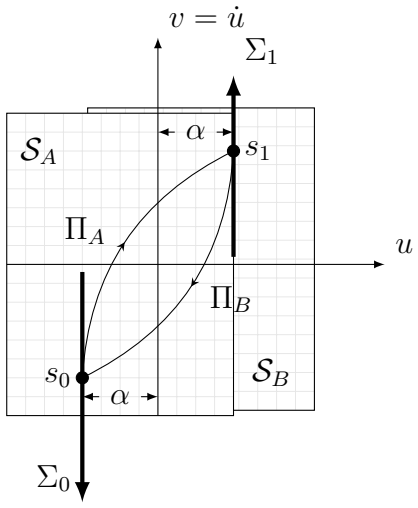

Figure 2.21: The Poincaré map $\Pi : \Sigma_0 \to \Sigma_0$ is the composition of the maps Π_A and Π_B.

more straightforward analysis. Let $u = x - \left(\frac{Rq_0}{2} + 1\right)$. Also, let $a - \left(\frac{Rq_0}{2} + 1\right) = \left(\frac{Rq_0}{2} + 1\right) - b = \alpha$. Then, the ODEs of Eq. (2.95) transform to the following.

$$\begin{cases} \ddot{u} + 2\varphi\dot{u} + u = \varphi q_0 & u < \alpha \qquad \mathcal{S}_A \\ \ddot{u} + 2\varphi\dot{u} + u = -\varphi q_0 & u > -\alpha \qquad \mathcal{S}_B \end{cases} \tag{2.97}$$

Notice that the transformation was chosen such that the substitution $(u, t) \longrightarrow (-u, t)$ only flips the index of the sheets. In other words, if the dynamics on sheet $\mathcal{S}_A$ are known, the dynamics on sheet $\mathcal{S}_B$ can be obtained by the substitution $(u, t) \longrightarrow (-u, t)$.

Let $\Sigma_0 = \{(u, v) \mid u = -\alpha, v < 0\}$, and $\Sigma_1 = \{(u, v) \mid u = \alpha, v > 0\}$. Let $s_0 = -v$ on Σ_0, and $s_1 = v$ on Σ_1. The section $\Sigma_0 \in \mathcal{S}_A$ is chosen to be the line upon which solutions exit $\mathcal{S}_B$ and enter $\mathcal{S}_A$, and Σ_1 is chosen to be the line upon which solutions exit $\mathcal{S}_A$ and enter $\mathcal{S}_B$. Let $\Pi_A : \Sigma_0 \longrightarrow \Sigma_1$, and $\Pi_B : \Sigma_1 \longrightarrow \Sigma_0$ be the maps defined by the ODEs (2.97). Then, the Poincaré map $\Pi = \Pi_A \circ \Pi_B$ is the composition of the Π_A and Π_B. These definitions are illustrated in Fig. 2.21. Because the behavior on one sheet is recoverable from the other after the substitution $(u, t) \longrightarrow (-u, t)$, The behavior of Π_A is the same as Π_B after swapping s_0 and s_1. We can write down the map Π_A as a parametric curve in the (s_0, s_1) plane by directly solving the governing ODE (2.97) with the

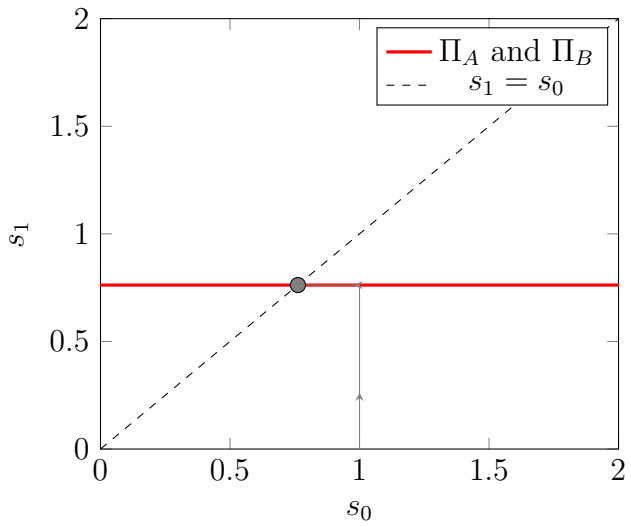

Figure 2.22: Lamerey's Diagram for the Piecewise-Hysteretic volume-dependent system, where $\alpha = 2$, $\varphi = 4$, and $q_0 = 2$. Clearly, the map Π_A has a fixed point, which means that there will be a limit cycle for this parameter set when plotted in the phase plane, since Π_B is equivalent to Π_A.

initial conditions $u(0) = u_0$, $v(0) = v_0$.

$$u(t) = e^{-\varphi t}\left((u_0 - \varphi q_0)\cosh \omega t + \left(\frac{v_0 + \varphi(u_0 - \varphi q_0)}{\omega}\right)\sinh \omega t\right) + \varphi q_0 \tag{2.98}$$

$$v(t) = e^{-\varphi t}\left(v_0 \cosh \omega t + \frac{1}{\omega}\left(-\varphi v_0 - (u_0 - \varphi q_0)\right)\sinh \omega t\right) \tag{2.99}$$

Now, let $u_0 = -\alpha$, and $v_0 = -s_0$. We are interested in the solution when $t = t_1$, satisfying $u(t_1) = \alpha$, $v(t_1) = s_1$.

$$\alpha = e^{-\varphi t_1}\left((-\alpha - \varphi q_0)\cosh \omega t_1 + \left(\frac{-s_0 + \varphi(-\alpha - \varphi q_0)}{\omega}\right)\sinh \omega t_1\right) + \varphi q_0 \tag{2.100}$$

$$s_1 = e^{-\varphi t_1}\left(-s_0 \cosh \omega t + \frac{1}{\omega}\left(\varphi s_0 + (\alpha \varphi q_0)\right)\sinh \omega t_1\right) \tag{2.101}$$

Once again, this is a linear system in s_0 and s_1 so we can solve for these variables individually. After lengthy algebraic manipulation, we reach the following solution.

$$\Pi_A : \begin{cases} s_0 = \frac{-\omega}{\sinh\tau}\left((\alpha-\varphi q_0)\,e^{\xi\tau} + (\alpha+\varphi q_0)\,(\cosh\tau+\xi\sinh\tau)\right) \\ s_1 = \frac{\omega}{\sinh\tau}\left((\alpha+\varphi q_0)\,e^{-\xi\tau} + (\alpha-\varphi q_0)\,(-\xi\sinh\tau+\cosh\tau)\right) \end{cases} \tag{2.102}$$

Here, $\xi = \frac{\varphi}{\omega} = \frac{\varphi}{\sqrt{\varphi^2-1}}$, and $\tau = \omega t_1$. Note that for $\varphi > 1$, then $\xi \in (1, \infty)$.

Because we have considered a case where the maps Π_A and Π_B have the same form, the Poincaré map can be represented on Lamerey's diagram by applying the transformation Π_A twice. Therefore, finding a fixed point in Π_A is a sufficient (but not necessary!) condition for there to be a fixed point in the Poincaré map. This process is illustrated in Fig. 2.22.

By determining the correspondence functions analytically, we have shown that this system exhibits a periodic solution that is globally-attracting whenever neither sheet contains its own equilibrium point, the condition set by Eq. (2.96). Figure 2.23 illustrates this globally-attracting limit cycle in the $(x, \dot{x})$ plane.

Now that we have shown that this model can exhibit a periodic steady-state solution, we must now understand how well this periodic solution matches the shape of the Lundberg A-waves. At first glance, it appears as if this solution in $\dot{x}$ matches the clinically-observed shape of the Lundberg A-wave waveform, categorized by exponential-like increases and decreases to two different values. However, because the input flow rate q changes depending on the sheet, the resulting pressure, $P(t) = Rq - R\dot{x}(t) + 1$, is not simply scaled by a constant. The waveform appears differently, illustrated by Figure 2.25.

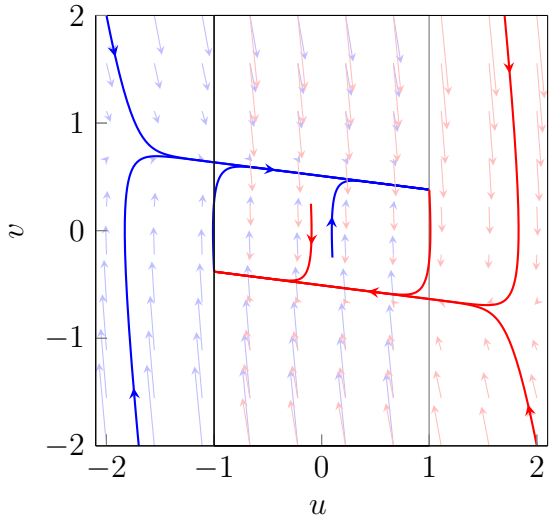

Figure 2.23: Phase portrait of piecewise-linear volume-dependent hysteretic system, where $\alpha = 1$, $\varphi = 4$, $q_0 = 1$. All solutions converge to the periodic orbit that spans both sheets $\mathcal{S}_A$ and $\mathcal{S}_B$. Individually, each sheet has the stability of a stable node that does not contain its own equilibrium point. As a result, the solutions switch sheets before they reach this equilibrium, and the steady-state behavior involves continuous switching between both sheets.

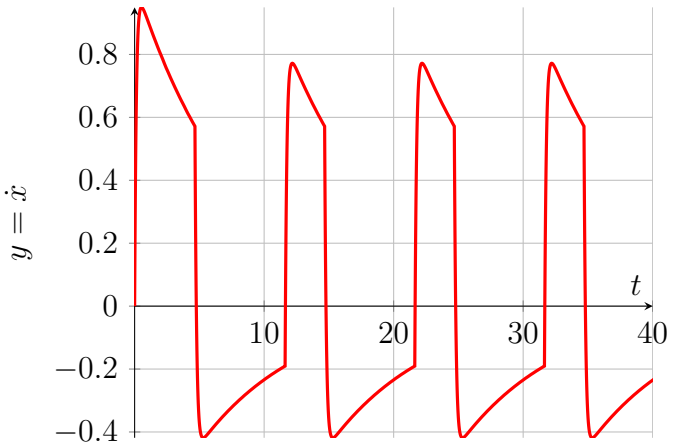

Figure 2.24: Time-Series plot of velocity for the piecewise-hysteretic position-dependent system when $\phi = 4$, $a = 3.5$, $b = 1.5$, ($\alpha = 1$), and $q_0 = 1$. While the shape of this waveform somewhat resembles that of the Lundberg A-Waves, make no mistake: this plot is of velocity versus time, and not pressure.

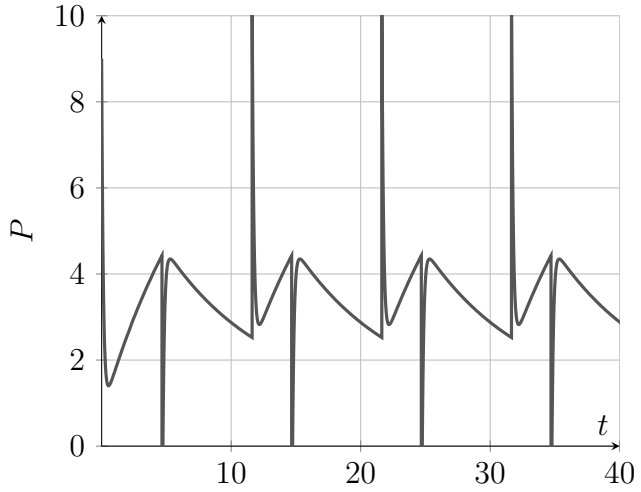

Figure 2.25: Time-Series plot of Pressure for the piecewise-hysteretic position-dependent system when $\phi = 4$, $a = 3.5$, $b = 1.5$, ($\alpha = 1$), and $q_0 = 1$. While the solution is indeed periodic, the qualitative shape of the waveform does not closely resemble Lundberg A-waves, represented in Fig. 2.26 even if the high-amplitude spikes are ignored.

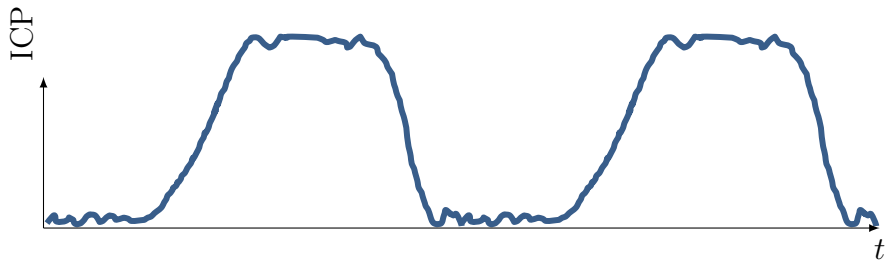

Figure 2.26: Reproduction by the author of the qualitative shape of the Lundberg A-Waves. The characteristic shape that is observed is a sharp increase to a high value of pressure, and then a sharp decrease to a low value of pressure.

Chapter 3
A Dual-Reservoir Model

The model that we built in the previous chapter contained one chamber: the volume of ventricular CSF that is surrounded by brain tissue. In the construction of that model, we implicitly made the assumption that only changes in the volume of CSF will change ICP and compress the surrounding brain tissue. We may find, when we experimentally test the model, that some effects external to the model cannot be neglected. In particular, since the volume of arterial blood within the skull changes with time, this causes deformation of brain tissue in a way that could affect ICP. Hence, in this chapter, we construct a dual-chamber model of ICP dynamics that includes a chamber for ventricular CSF coupled to a chamber for arterial blood. This is constructed in a way similar to the previous model, by applying the first-principle laws of the balance of mass and linear momentum to each fluid chamber and the tissue. Once we obtain the governing equations for this model, we analyze the possible qualitative dynamic behaviors that this system is capable of, paying special attention to the stability of the equilibrium point. We conclude by providing rough estimates for the parameter values in the model, and show that the steady-state value of ICP lies within a healthy range for a patient.

3.1 Governing Equations

The mechano-hydraulic model proposed here is made of two hydraulic systems (ventricular csF and arterial blood) and two mechanical systems (brain tissue and arteries). The governing equations are obtained from the balance of mass of each fluid chamber, and the balance of linear momentum of the effective masses of the mechanical systems.

Because CSF is produced from arterial blood, any volume of fluid that is added to the CSF chamber must be removed from the arterial blood chamber. This process depends on the difference in arterial blood pressure, P_A, and intracranial pressure, P_B. From here on, the subscript A refers to "artery", and B refers to "brain". We idealize this process as a constant CSF formation rate, I, along with a component that is linear to the pressure gradient, which is represented by the volumetric fluid resistor with value R_f. After accounting for this adjustment to the CSF formation rate, the balance of mass for the ventricular CSF compartment is similar to that obtained in Chapter 2, Eqn. 2.2.

$$\frac{P_v - P_B}{R_o} + \frac{P_A - P_B}{R_f} + I = A_B \dot{u}_B \,, \tag{3.1}$$

where P_v is the venous blood pressure, R_o is the volumetric fluid resistance to resorption, A_B is the effective surface area of the brain tissue, u_B is the generalized deformation coordinate for the effective mass of the brain, and the overdot indicates the derivative with respect to time.

We can construct a similar equation for the balance of mass of the arterial blood chamber. The flow of arterial blood through blood vessels resembles the flow of a viscous fluid through a cylindrical pipe. The Hagen-Poiseuille law states that these flow rates are proportional to the pressure gradients across the pipe. Hence, we state that the flow of arterial blood into the arterial chamber is proportional to the pressure difference between the extracranial arterial blood pressure P_o and the arterial blood pressure P_A, where we write the proportionality constant as $1/R_a$. Similarly, the flow of blood out of the arterial blood chamber will be proportional to the pressure difference between P_A and P_v, where we write the proportionality constant as $1/R_c$. In a way similar to the ventricular CSF compartment, we equip the boundary of the arterial blood chamber with an effective surface area A_A and generalized deformation coordinate u_A. Thus, the balance of mass for the arterial blood chamber is

$$\frac{P_o - P_A}{R_a} + \frac{P_v - P_A}{R_c} + \frac{P_B - P_A}{R_f} - I = A_A \dot{u}_A \,. \tag{3.2}$$

The arterial blood chamber is surrounded by the effective mass of the arteries, m_A, and the ventricular CSF chamber is surrounded by the effective mass of the

brain tissue. However, since the arterial walls directly border the brain tissue, the motion of the masses are coupled to one another. We idealize the arterial wall as a viscoelastic material, with intrinsic stiffness k_A and damping η_A that is described with the KV model. Like in the previous model, the brain tissue is also described with the KV model with stiffness k_B and damping η_B. Because an increase in the volume of the arteries can also cause a compression in the surrounding brain tissue, we connect the KV spring k_B and dashpot η_B for the brain to the arterial wall. After applying the balance of linear momentum to the effective mass of the arterial wall, we have

$$m_A\ddot{u}_A + \eta_A\dot{u}_A + \eta_B(\dot{u}_A + \dot{u}_B) + k_A u_A + k_B(u_A + u_B) = P_A A_A\,, \tag{3.3}$$

and by applying it to the effective mass of the brain, we have

$$m_B\ddot{u}_B + \eta_B(\dot{u}_A + \dot{u}_B) + k_B(u_A + u_B) = P_B A_B\,. \tag{3.4}$$

Equations (3.3) and (3.4), when written in matrix notation, take on the following form:

$$\mathsf{M}\ddot{\mathbf{u}} + \mathsf{C}\dot{\mathbf{u}} + \mathsf{K}\mathbf{u} = \mathsf{A}\mathbf{P}\,, \tag{3.5}$$

where $\mathbf{u} = \begin{bmatrix} u_A \\ u_B \end{bmatrix}$ is defined as the column vector of configuration variables. However, since the pressures P_A and P_B are linear functions of the velocities $\dot{\mathbf{u}}$, as given by Eqns. (3.2) and (3.1), the vector of pressures $\mathbf{P} = \begin{bmatrix} P_A \\ P_B \end{bmatrix}$ can be written in the following form:

$$\mathbf{P} = \boldsymbol{\phi} + \mathsf{E}\dot{\mathbf{u}}\,, \tag{3.6}$$

where $\boldsymbol{\phi}$ is a 2×1 vector of constants and E is a 2×2 matrix of constants, neither of which depend on $\boldsymbol{u}$ or its time derivatives. Let us define a new coordinate $\mathbf{x}$ that is the deviation from the static equilibrium point, which occurs at ($\ddot{\mathbf{u}} = \mathbf{0}$, $\dot{\mathbf{u}} = \mathbf{0}$).

$$\mathbf{x} = \mathbf{u} - \mathsf{K}^{-1}\mathsf{A}\boldsymbol{\phi} \tag{3.7}$$

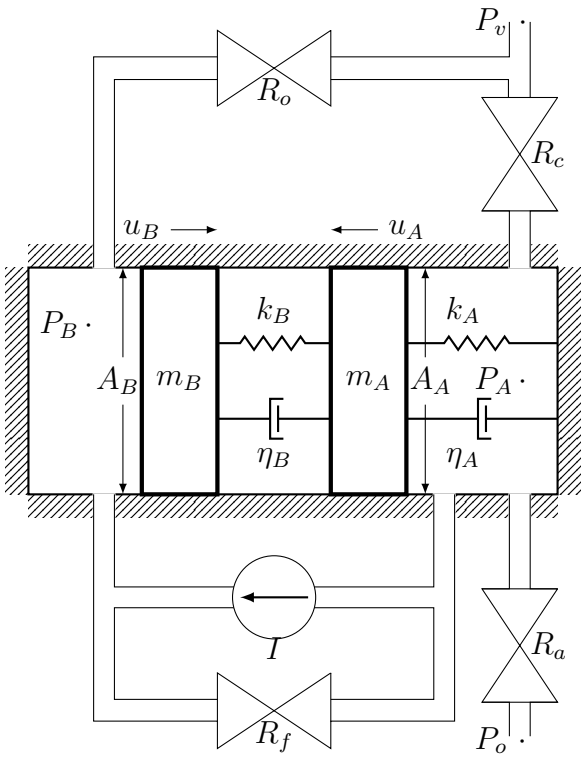

Figure 3.1: Schematic of the proposed mechano-hydraulic system. The arterial blood chamber has pressure P_A, the effective mass of the arterial wall is m_A, the KV effective springs and dashpots of the arterial wall are k_A and η_A respectively, the arterial chamber has effective surface area A_A and displacement u_A. The ventricular CSF chamber has pressure P_B, the effective mass of the brain tissue is m_B, the KV effective springs and dashpots of the brain tissue are k_B and η_B respectively, the ventricular CSF chamber has effective surface area A_B and displacement u_B. The extracranial arterial blood pressure is P_o and the venous blood pressure is P_v. The constant CSF formation rate is I, and R_f is the volumetric fluid resistance to pressure-driven CSF formation. The volumetric fluid resistances for the arteries, capillaries, and CSF resorption are R_a, R_c, and R_o respectively.

We find that we can combine Equations (3.5), (3.6), and (3.7) in the following form.

$$\mathsf{M}\ddot{\mathbf{x}} + (\mathsf{C} - \mathsf{AE})\,\dot{\mathbf{x}} + \mathsf{K}\mathbf{x} = \mathbf{0} \tag{3.8}$$

3.2 Dynamic Analysis of Governing Equations

Since the pressures P_A and P_B are only algebraic functions of $\dot{u}_A$ and $\dot{u}_B$, we expect that features of the solutions in $\mathbf{u}$ and $\dot{\mathbf{u}}$ will transfer directly to the solutions in P_A and P_B. In particular, we are referring to the number and stability type of equilibrium points. System (3.8) has a four-dimensional state-space: two state variables are the positions u_A and u_B, while the other two are the velocities $\dot{u}_A$ and $\dot{u}_B$. Let

$$\dot{\mathbf{x}} = \mathbf{v}\,, \tag{3.9}$$

which allows us to write the system (3.8) in state-variable form as a first-order system as follows.

$$\begin{bmatrix} \dot{\mathbf{x}} \\ \dot{\mathbf{v}} \end{bmatrix} = \begin{bmatrix} 0 & 1 \\ -\mathsf{M}^{-1}\mathsf{K} & -\mathsf{M}^{-1}\left(\mathsf{C} - \mathsf{AE}\right) \end{bmatrix} \begin{bmatrix} \mathbf{x} \\ \mathbf{v} \end{bmatrix}\,. \tag{3.10}$$

The elements of the matrix in Eqn. (3.10) are 2×2 block matrices, where $\mathsf{1}$ is the 2×2 identity matrix. Since this is a linear system, it has one and only one equilibrium point, which is located at the origin [19]. If this equilibrium is stable, then the steady-state solution is the solution that begins at the origin and remains at the origin for all time. This equilibrium point does not correspond to zero pressure, rather it refers to how far the deformations $\mathbf{u}$ are displaced from their equilibrium value, $\mathsf{K}^{-1}\mathsf{A}\boldsymbol{\phi}$.

To get a sense of the predicted equilibrium value of steady-state intracranial pressure for this model, we would first need a good sense of the value of each model parameter. Unfortunately, many of the material properties required by our model are extremely difficult to accurately measure on living tissue. Acceptable values are still being agreed upon by the research community. Nevertheless, in order to continue this analysis, we proceed with a best estimate of these model parameters and the value for steady-state ICP that they predict. Since the flow rates that are proportional to a pressure gradient resemble the resistors of the Ursino-Lodi model, [8], we used the values reported in their paper for our fluid resistors as well. For the Kelvin-Voigt springs and dashpots, we used the values reported in [22] and [23] for the spring and damping coefficients of the brain,

Table 3.1: Parameter values for the dual-chamber model

Parameter Name	Symbol	Value [Reference]
Spring Coefficient of Arteries	k_A	10^5 N/m [21]
Spring Coefficient of Brain (KV)	k_B	1750 N/m [22]
Damping of Arteries	η_A	10^2 N $\cdot$ s/m [N/A]
Damping of Brain (KV)	η_B	10^9 N $\cdot$ s/m [23]
Formation Rate of CSF	I	6×10^{-9} m^3/s [7]
Fluid Resistance of Arteries	R_a	800×10^6 Pa $\cdot$ s/m^3 [8]
Fluid Resistance of Capillaries	R_c	800×10^6 Pa $\cdot$ s/m^3 [8]
Fluid Resistance to CSF Formation	R_f	317×10^6 Pa $\cdot$ s/m^3 [8]
Fluid Resistance to CSF resorption	R_o	70×10^9 Pa $\cdot$ s/m^3 [8]
Arterial Boundary Surface Area	A_A	1×10^{-3} m^2 [N/A]
Ventricular Boundary Surface Area	A_B	1×10^{-2} m^2 [N/A]

respectively. To obtain a rough estimate of the stiffness of the arterial wall, k_A, we consider an elastic hollow cylinder with initial internal radius $r_0 = 0.5$ cm, thickness $t = 0.6$ mm, effective length $L = 1$ m, and modulus of elasticity $E = 80$ kPa [21]. With uniform internal pressure loading, the stress in the walls is

$$\sigma = \frac{pr}{t} = \frac{F}{tL} \tag{3.11}$$

while the strain in the walls is

$$\epsilon = \frac{2\pi(r - r_0)}{2\pi r_0} = \left(\frac{r}{r_0} - 1\right) . \tag{3.12}$$

If we assume that the arterial wall is a linear elastic solid, its constitutive relation is given by Hooke's law:

$$\sigma = E\epsilon\,, \tag{3.13}$$

then we can define the spring coefficient k_A to be

$$k_A = \frac{ELt}{r_0} \tag{3.14}$$

The equilibrium value of pressure is given by Eqn. (3.6), when $\dot{\mathbf{u}} = \mathbf{0}$. When considering the parameter values of Table 3.1, we have

$$P_{eq} = \begin{bmatrix} P_{A,eq} \\ P_{B,eq} \end{bmatrix} = \begin{bmatrix} 7.041\text{kPa} \\ 2.255\text{kPa} \end{bmatrix} \tag{3.15}$$

This steady-state value of pressure predicted by the dual-chamber model is one that lies within the range of ICP observed in healthy patients [3].

To determine the stability of the equilibrium point, we can examine the eigenvalues of the 4×4 matrix in Eqn. (3.10). If any of the eigenvalues have a positive-real part, then the steady-state solution is unstable [19]. Unfortunately, since the size of the system matrix in Eqn. (3.10) is 4×4, the characteristic equation is a quartic polynomial. Although the solution to a quartic polynomial can be written in closed form, it is too unwieldy to practically use. Therefore, in order to proceed with the analysis, we set the model parameters to those presented in Table 3.1, and numerically calculated the eigenvalues of the 4×4 matrix in Eqn. (3.10). For this configuration, we found that the eigenvalues were all negative, and therefore the configuration was stable. Then, we selected one parameter and varied it over several orders of magnitude, while keeping the others fixed, numerically evaluating the eigenvalues at each point. This process was the repeated for all of the model parameters shown in Table 3.1. This method of exploring the parameter space found no points that yielded eigenvalues with positive-real part, and therefore, we found no parameter sets that cause the only equilibrium point to lose its stability. We were only able to find unstable configurations by expanding the parameter space to include physically unrealistic values. For example, a negative value for either Kelvin-Voigt spring stiffness would cause a loss of stability in the equilibrium point.

The phase portraits presented in this section are ones that are created with

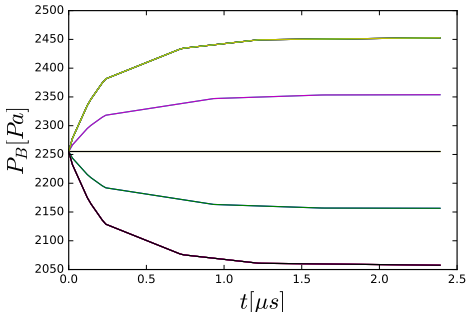

(a) Response of P_B to a nonzero initial displacement at time $t = 0$. The solutions very quickly approach a non-equilibrium value. This is a zoomed-in version of Fig. 3.2b for values of t very close to zero.

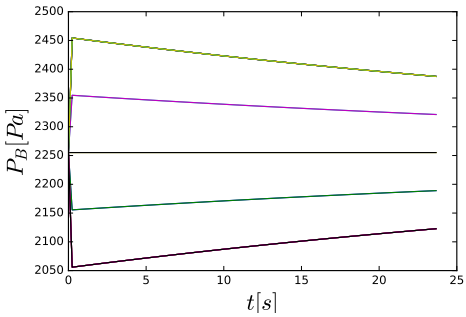

(b) Response of P_B to a nonzero initial displacement at time $t = 0$. After quickly approaching a different value, these solutions slowly return back to the equilibrium value.

Figure 3.2: Family of time-series responses of the intracranial pressure P_B to a nonzero initial displacement at time $t = 0$. Each line in both Fig. 3.2a and Fig. 3.2b corresponds to a different initial displacement. Figure 3.2a shows the dynamic response on very short time scales, while Fig. 3.2b shows the response over a larger time scale.

the model parameter values set to those presented in Table 3.1. The behavior we observe in the phase space is indicative of two different time scales acting simultaneously. Figures 3.2b and 3.2a illustrate this behavior. In response to an initial condition with nonzero position yet zero velocity, the pressure P_B exponentially increases to a value on the order of microseconds (Figure 3.2a). Figure 3.2b is a zoomed-out version of Fig. 3.2a. Here we see that P_B is observed to start returning to its equilibrium value on the order of seconds. Figures 3.3a and 3.3b share initial conditions where at $t = 0$, $u_A = u_B = 0$ and where v_A and v_B are nonzero. The initial values of v_A and v_B for each solution path are shown on the border of Figure 3.3b. It is apparent that, at a very fast time scale, the dynamics quickly converge onto a manifold of lower dimension.

The value of ICP that this dual-chamber model predicts for a healthy steady-state is near what would be measured in a healthy patient. However, the dynamic response back to this equilibrium after an external impulse appears to act over two very different time scales. As a response to a change in the volume of CSF, the pressure P_B changes very quickly, but then very slowly returns to its equilibrium

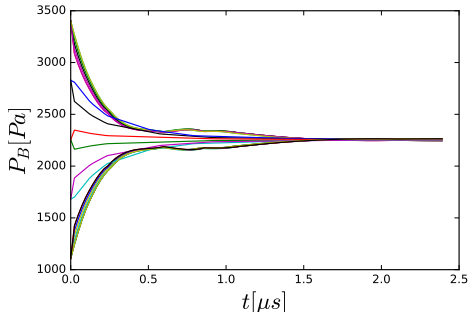

(a) Family of transient responses in the intracranial pressure P_B to a nonzero initial velocity at time $t = 0$. Each curve begins with a different initial condition, but then approaches a steady-state value of pressure as time approaches infinity.

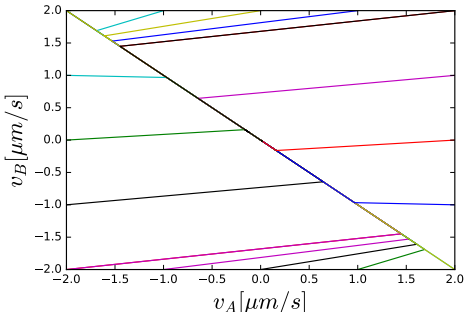

(b) Projection of the four-dimensional phase space onto the $v_A - v_B$ plane. All initial conditions, which begin on the border, have initial conditions of $u_A = u_B = 0$, with v_A and v_B as shown on the border of the plot. All of the solutions then rapidly approach a weakly-stable manifold, and then eventually approach the orgin.

Figure 3.3: Two plots of the system response to a nonzero initial velocity condition. Figure 3.3a shows a family of responses to these conditions, and Fig. 3.3b shows these plotted in the projection of the four-dimensional phase space. Both figures are different ways to interpret the same solution, and they retain the same qualitative features. After a rapid initial transient, the solutions converge onto a steady-state value.

value. Because these time scales are so different, we may be able to reduce the dimension of this model with no sacrifice in the accuracy of its predictions. Alternatively, this behavior may be an artifact of the model parameter values that we selected for this analysis. **Since this model is linear, it is not capable of exhibiting limit cycles**.

Chapter 4
Discussion and Conclusions

In this thesis, we have developed two mathematical models to study intracranial pressure (ICP) dynamics. Instead of being built from electric circuit analogs, both of these models consist of hydraulic systems coupled to mechanical systems. As a result, they allow for a proper use of the first principles of the balance of mass and the balance of linear momentum.

The first of these models consisted of a single chamber that contained ventricular CSF and was bordered by brain tissue. By specifying the formation rate, absorption rate, and storage behaviors of CSF, as well as specifying the mechanical behavior of the surrounding tissue, we obtained the governing equations of the model from the balance laws of mass and linear momentum. Then we analyzed the dynamic behavior of a non-dimensional form of these equations. First, we explored the linear case, where the only behavior that we observed was an asymptotic return to an equilibrium value of pressure and deformation (equivalently, volume of CSF). Because this could not exhibit limit cycles in the phase space, this model is incomplete. As a result, we postulated several different mechanisms of CSF production, which we allowed to vary with either pressure or position. These laws were piecewise, so we were faced with piecewise-linear dynamical systems for their mathematical analysis. We carried out the analysis for each system while paying special attention to the existence or non-existence of limit cycles in the state space.

In the case where the CSF formation rate varied with pressure, with or without hysteresis, the only possible steady-state solutions were constant. While potentially capable of explaining steady-state healthy and elevated ICP levels, these models, along with the unmodified linear model, would be incapable of describing the case of oscillatory ICP (Lundberg A-Waves). Only one governing law for the

CSF formation rate that we analyzed had the potential for limit cycle solutions: this required the CSF formation rate to vary hysteretically as a function of position. This model could explain low and high values of ICP, as well as oscillatory ICP, as a result of change in the parameters.

One interpretation for these findings is the following explanatory hypothesis for the mechanism by which Lundberg A-Waves are formed. Under unusually high CSF volumes (state x in the model), the brain ceases production of CSF in an effort to regulate pressure and CSF volume within the skull. The CSF production does not resume until the volume returns to a healthy level, lower than the volume that caused CSF production to cease. If we suppose that this regulatory mechanism is always present, we can still reconcile that we do not observe oscillatory behavior in healthy patients. Under low (normal) values of the resistance to CSF absorption, this model predicts a steady-state equilibrium value of ICP, consistent with observation. Elevated ICP in patients with traumatic brain injury (TBI) is known to occur when either the resistance to CSF absorption becomes too high or the CSF formation rate becomes too high. This model explains these behaviors well. Lundberg A-waves seldom occur in patients who have otherwise-healthy ICP levels. In this model, steady-state periodic behaviors are only observed when the resistance to CSF absorption (R) exceeds some critical value. This would be consistent with the clinical observation that A-Waves occur spontaneously, especially in patients with TBI. This critical value of R would be dependent on the postulated threshold pressures. The value of these threshold pressures, and even their existence, would need to be understood as an idealization of some other control mechanism of the brain.

In order to draw any clinically-helpful conclusions from this model, we would need to closely compare it to experiments and measured clinical data. Currently, we have not been able to match the waveforms we have obtained to the shape of those observed clinically. We will want to investigate whether data can be matched by only changing the values of parameters, and not by modifying the governing equations. At this point, we will be faced with one of two outcomes. One case is that the model will be incapable of describing the new scenarios we have posed, and we will need to further edit and refine the governing equations. Alternatively, we will expand the predictive realm of the model, and will offer more evidence to the hypotheses we have chosen.

Since the analogous rate law that depended on pressure instead of volume did not cause limit cycles, we may be able to draw the conclusion that the CSF formation rate is controlled by volume (strain, deformation), and not pressure directly. This would be an interesting statement to make, and its validity would be dependent on how well we are able to match data to this model in the future. Currently, the qualitative shape of limit cycles we found in the single-chamber model does not perfectly match the characteristic shape of the observed Lundberg A-Waves. However, obtaining this might be just a matter of tuning parameters in order to get this shape, and may not require a complete overhaul of the model. Our future work will involve a deeper investigation of this. The conclusions concerning Lundberg A-Waves that we wish to draw with our work must be tested against the leading hypothesis of their formation. Currently, the leading hypothesis is that of the so-called vasodilatory cascade, where the brain's autoregulation of the arterial blood flow, coupled with other effects causes a feedback loop resulting in instability [3]. The work we have presented here could offer an alternative hypothesis to this one. In addition, we may find similar results by considering piecewise variations in different model parameters, such as the outflow resistance, or of the Kelvin-Voigt equivalent spring.

The second model that we discussed in this thesis consisted of two chambers: one for ventricular CSF and the other for arterial blood. This construction resulted in a model with a four-dimensional state space. Because the state space of this model was four-dimensional, we were limited in the amount of analytic analysis we could perform. Therefore, we picked values of the model parameters that represented the best available approximations, and performed our analyses numerically. We found that the steady-state value of intracranial pressure that the dual-chamber model predicted had agreed well with the range for a healthy patient. Then, we found that the equilibrium point was a stable node for the reported model parameter values. However, we found that the dynamic behavior responded on two different time scales, where the one was fast and the other was slow. This behavior might be the result of picking up erroneous values for the model parameters. Alternatively, this might indicate that we can reduce the order of this model in our future work. Doing this would be very beneficial, as it would allow for easier analysis of the model without sacrificing accuracy.

Bibliography

[1] Nelson, G. E., G. G. Robinson, and R. A. Boolootian (1974) "Fundamental concepts of biology," .

[2] Kyriacou, S. K., A. Mohamed, K. Miller, and S. Neff (2002) "Brain mechanics for neurosurgery: modeling issues," *Biomechanics and Modeling in Mechanobiology*, **1**(2), pp. 151–164.

[3] Suarez, J. I. (2004) *Critical Care Neurology and Neurosurgery*, Springer, New York.

[4] Goldsmith, W. (2001) "The state of head injury biomechanics: past, present, and future: part 1," *Critical Reviews in Biomedical Engineering*, **29**(5&6).

[5] Cutler, R., L. Page, J. Galicich, and G. Watters (1968) "Formation and absorption of cerebrospinal fluid in man," *Brain*, **91**(4), pp. 707–720.

[6] Paulson, O., S. Strandgaard, and L. Edvinsson (1989) "Cerebral autoregulation." *Cerebrovascular and brain metabolism reviews*, **2**(2), pp. 161–192.

[7] Marmarou, A., K. Shulman, and R. M. Rosende (1978) "A nonlinear analysis of the cerebrospinal fluid system and intracranial pressure dynamics," *Journal of Neurosurgery*, **48**(3), pp. 332–344.

[8] Ursino, M. and C. A. Lodi (1997) "A simple mathematical model of the interaction between intracranial pressure and cerebral hemodynamics," *Journal of Applied Physiology*, **82**(4), pp. 1256–1269.

[9] Guinane, J. (1972) "An equivalent circuit analysis of cerebrospinal fluid hydrodynamics," *American Journal of Physiology–Legacy Content*, **223**(2), pp. 425–430.

[10] Lim, S. T., D. G. Potts, V. Deonarine, and M. D. Deck (1973) "Ventricular compliance in dogs with and without aqueductal obstruction," *Journal of neurosurgery*, **39**(4), pp. 463–473.

[11] Kashif, F., T. Heldt, and G. Verghese (2008) "Model-based estimation of intracranial pressure and cerebrovascular autoregulation," in *Computers in Cardiology, 2008*, IEEE, pp. 369–372.

[12] Linninger, A. A., M. Xenos, B. Sweetman, S. Ponkshe, X. Guo, and R. Penn (2009) "A mathematical model of blood, cerebrospinal fluid and brain dynamics," *Journal of mathematical biology*, **59**(6), pp. 729–759.

[13] Lakin, W. D., S. A. Stevens, B. I. Tranmer, and P. L. Penar (2003) "A whole-body mathematical model for intracranial pressure dynamics," *Journal of mathematical biology*, **46**(4), pp. 347–383.

[14] Hakim, S., J. G. Venegas, and J. D. Burton (1976) "The physics of the cranial cavity, hydrocephalus and normal pressure hydrocephalus: mechanical interpretation and mathematical model." *Surgical Neurology*, **5**(3), pp. 187–210.

[15] Nagashima, T., N. Tamaki, S. Matsumoto, B. Horwitz, and Y. Seguchi (1987) "Biomechanics of hydrocephalus: a new theoretical model." *Neurosurgery*, **21**(6), pp. 898–904.

[16] Sobey, I., A. Eisenträger, B. Wirth, and M. Czosnyka (2012) "Simulation of cerebral infusion tests using a poroelastic model," *Int. J. Numer. Anal. Model., Ser. B*, **3**, pp. 52–64.

[17] Hasan M.D., M. and C. S. Drapaca "A Poroelastic-Viscoelastic Limit for Modeling Brain Biomechanics," .

[18] Tenti, G., S. Sivaloganathan, and J. M. Drake (2008) "Mathematical modeling of the brain: Principles and challenges," *Neurosurgery*, **62**(5), pp. 1146–1157.

[19] Jordan, D. W. and P. Smith (2007) *Nonlinear Ordinary Differential Equations, Fourth Edition*, Oxford University Press.

[20] Andronov, A. A., A. A. Vitt, and S. E. Khaikin (1966) *Theory of Oscillators*, Dover, New York.

[21] Tanaka, M., M. Sugawara, Y. Ogasawara, T. Izumi, K. Niki, and F. Kajiya (2013) "Intermittent, moderate-intensity aerobic exercise for only eight weeks reduces arterial stiffness: evaluation by measurement of stiffness parameter and pressure–strain elastic modulus by use of ultrasonic echo tracking," *Journal of medical ultrasonics*, **40**(2), pp. 119–124.

[22] Kruse, S. A., G. H. Rose, K. J. Glaser, A. Manduca, J. P. Felmlee, C. R. Jack, and R. L. Ehman (2008) "Magnetic resonance elastography of the brain," *Neuroimage*, **39**(1), pp. 231–237.

[23] Hasan, M. and C. S. Drapaca (2015) "A Poroelastic-Viscoelastic Limit for Modeling Brain Biomechanics," in *MRS Proceedings*, vol. 1753, Cambridge Univ Press, pp. mrsf14–1753.